https://doi.org/10.1016/j.jpowsour.2019.227276

A Novel Selenium-Phosphorous Amorphous Composite by Plasma Assisted Ball Milling for High-Performance Rechargeable Potassium-Ion Battery Anode

Cheng Lin[a], Liuzhang Ouyang[a,b]*, Chaojin Zhou[a], Renzong Hu[a,b], Lichun Yang[a], Xusheng Yang[c,d]*, Huaiyu Shao[e], Min Zhu[a,b]

[a]*School of Materials Science and Engineering, Guangdong Provincial Key Laboratory of Advanced Energy Storage Materials, South China University of Technology, Guangzhou, 510641, People's Republic of China*

[b]*China-Australia Joint Laboratory for Energy & Environmental Materials, Key Laboratory of Fuel Cell Technology of Guangdong Province, Guangzhou, Guangzhou, 510641, People's Republic of China*

[c]*Department of Industrial and Systems Engineering, The Hong Kong Polytechnic University, Hung Hom, Kowloon, Hong Kong, China*

[d]*Hong Kong Polytechnic University Shenzhen Research Institute, Shenzhen 518057, China*

[e]*Joint Key Laboratory of the Ministry of Education, Institute of Applied Physics and Materials Engineering (IAPME), University of Macau, Taipa, Macau SAR, China*

**Corresponding author E-mail address: meouyang@scut.edu.cn (Liuzhang Ouyang); xsyang@polyu.edu.hk（Xu-Sheng Yang）*

Abstract:

Potassium-ion batteries (PIBs) are becoming one of the promising alternative metal-ion battery systems to lithium-ion batteries due to the abundance and low cost of potassium. Among the anode materials for the metal-ion battery systems, phosphorus-based materials are attractive due to the low cost and their high theoretical-specific capacity. Herein, for the first time, we report the selenium -phosphorous-carbon (Se-P-C) amorphous composites prepared by the plasma-assisted ball milling method as the high-performance anode material for PIBs. In particular, when the amorphous Se-P composite anode with the molar ratio of 1:2 and the P-milling time of 30 h (Se-2P/C@30h), the associated PIB delivers a high reversible capacity of 634 mA h g^{-1} at a current density of 0.05 A g^{-1} and excellent rate capability of 248.6 mA h g^{-1} at a current density of 1 A g^{-1}. Furthermore, the experimental characterization and analysis reveal the reaction mechanisms that K−P (K_2P_3) and K−Se (KSe) phases are formed during the potassiation process. The present work provides a facile approach to achieve a promising anode material for

K-ion batteries, and the preparation route can be viewed as a reference for the further development of phosphorous-based anodes with high capacity and long cycle life for PIBs.

Keywords: Se-P-C composite; promising anode; potassium-ion battery; plasma-assisted ball milling;

1. Introduction

Nowadays, lithium-ion batteries (LIBs) have been more and more widely utilized in energy applications, such as hybrid electric vehicles and portable devices, etc. However, the uneven distribution and limited capacity of Li resources around the world (0.002 wt. % in the earth crust and 0.18 mg l^{-1} in ocean) [1] are compelling researches to explore new abundant metallic elements for the development of alternative battery systems. For example, the abundant metals such as Na [2-3], K [4], Al [5], Mg [6] and Ca [7-8] are quietly attractive. It seems that the potassium-ion batteries (PIBs) system possesses relatively low performance among the alkali metal-based battery systems, due to the lower energy density and large ion radius of K (685 mA h g^{-1} and 1.38 Å), compared with that of Li (3361 mA h g^{-1} and 0.68 Å) and Na (1161 mA h g^{-1} and 0.97 Å), respectively. Nonetheless, it should be noted that the standard hydrogen potential of K (- 2.93 V vs E^o) is lower than that of Na (- 2.71 V vs E^o) and closer to that of Li (- 3.04 V vs E^o), indicating that PIBs are actually promising as the low-cost batteries with the high voltage and energy density. Moreover, unlike the poor intercalation ability of Na ions (35 mA h g^{-1} by forming

Na_6C_{64}) [9-10] into graphite, K ions show reversible intercalation/de-intercalation into graphite [11-12], soft/hard carbon [13-14] and graphene [15] as well.

Nonetheless, other anode materials are also being investigated to achieve the higher capacity, as the reported highest capacity for carbon-based materials is only 273 mA h g^{-1} [16]. For example, Zhao *et al.* [17] reported a rechargeable potassium-sulfur battery which could deliver a high capacity of 329.3 mA h g^{-1} after 50 cycles, however, it faced a serious capacity fading due to the production of polysulfides during cycling. As Se element possesses better electrical conductivity ($\approx 10^{-5}$ S cm^{-1}) and high theoretical specific capacity (678 mA h g^{-1}), Liu *et al.* [18] prepared a high-performance potassium-selenium (K−Se) battery and it exhibited outstanding cycle stability. However, pure Se is still subjected to the fast capability fading because of the dissolution of polyselenide intermediates in electrolytes. Meanwhile, the alloy-based anode materials started to be investigated. Sultana *et al.* [19] reported that Sn/C composite as anode material in PIBs delivered only 150 mA h g^{-1}, which is even worse than carbon material, at a current density of 25 mA g^{-1}. Sultana *et al.* [20] synthesized black phosphorous (P) as the anode for potassium battery and it showed 300 mA h g^{-1} even at a current density of 2 A g^{-1}, but the expensive price of black phosphorus limits its further development. Red phosphorous is treated as a promising anode for PIBs due to its low price and high theoretical potassium storage capacity (K_3P, 2595 mA h g^{-1}). However, the low conductivity and large volume expansion lead to the poor potassium storage electrochemical performance of red phosphorous. In order to solve the above problems, elements with higher conductivity can be

introduced to enhance the overall conductivity of the anode material and restrain the volume expansion in the potassium storage process. Zhang *et al.* [21] found that P-based alloy Sn_3P_4 exhibited better potassium storage performance than Sn and red phosphorous since the K−Sn and K−P alloy intermediate phase, which act as mutual buffers to alleviate the volume changes during cycling, were formed in the discharge process. Compared with Sn, Se shows smaller volume change in potassium storage process. Interestingly, Se-P phase shows better conductivity, compared with red phosphorous, and avoids the formation of polyselenide during charge and discharge process [22]. To the best of our knowledge, however, Se-P composite has not yet been reported as electrode materials for PIBs.

Actually, selenium phosphide (Se_xP_{1-x}, $0.2 < x < 1.0$), which can be synthesized by the melt-quenching method or the ball-milling technique, has been widely applied in electrical switches, display devices, and computer memories, owing to the good optical and semi-conductive properties [23]. Herein, for the first time, we reported the electrochemical performance of novel Se-2P/C amorphous composites synthesized via plasma-assisted ball milling (P-milling) method as anode material for PIBs. The P-milling method offers a simple, cost-effective and pollution-free method for preparing nanomaterials. It accelerates mechano-chemical reactions to pave the way for the future large-scale production of energy storage materials [24-25]. The structural and electrochemical properties were analyzed by X-ray diffraction (XRD), Raman spectroscopy, scanning electron microscope (SEM), transition electron microscope (TEM), and electrochemical measurements. When the amorphous Se-P

composite anode with the molar ratio of 1:2 and the P-milling time of 30 h (Se-2P/C@30h), the associated PIB delivered a high reversible capacity of 634 mA h g^{-1} at a current density of 0.05 A g^{-1} and excellent rate capability of 248.6 mA h g^{-1} at a current density of 1 A g^{-1}. Furthermore, reaction mechanisms were revealed that K−P (K_2P_3) and K−Se (KSe) phases are formed during the potassiation process. The present work provides a facile approach to achieve a promising anode material for PIBs.

2. Experimental

2.1 Materials synthesis

The worm-like expanded graphite (EG) was first obtained by calcining the expandable graphite (Qindao Xinghua Graphite Products Co., Ltd, ⩾ 99%, 100 mesh) at temperature of 1000 °C for 15 min at 5 °C/min under Ar atmosphere. Then, the raw materials of Se (Aladdin, ⩾ 99.9%, 200 mesh), red phosphorus (Aladdin, ⩾ 98.5%), and EG were mixed with the weight ratio of Se: P: C = 44.8: 35.2: 20 (i.e., the molar ratio of Se and P is 1:2) and placed in a stainless steel vial to synthesize the Se-2P/C composite powder via the P-milling method. Stainless steel balls were sealed with the mixture under Argon atmosphere and the weight ratio of the ball to powder was 50:1. The synthesis of the Se-P-C composite by P-milling is schematically illustrated in the Fig. 1. During the P-milling process, the mechanical energy, electron impact and heating impact are generated and exerted on the powder of Se, P and EG. Consequently, the amorphous carbon proceeded from the exfoliation and grind of EG

[26] and carbon coated Se-P composite nanoparticles structure can be in-situ formed in the P-milling process. The more details and mechanism of the P-milling process were explained and described in our previous paper [27-28]. In the present work, ball milling cylinder was vibrated with a double amplitude of 7 mm and a frequency of 16 Hz with the voltage of 15 kV, the current of 1.5 A and the discharge frequency of 60 kHz, respectively. Finally, two types of Se-2P/C composites, i.e., Se-2P/C@20h and Se-2P/C@30h, were achieved by P-milling under above P-milling condition with process times of 20 h and 30 h, respectively. In addition, the same P-milling condition with process times of 30 h were also used to synthesize other several types of Se-P composites, i.e., Se-P/C@30h (weight ratio of Se: P: C = 57.46: 22.54: 20), Se-4P/C@30h (weight ratio of Se: P: C = 31.14: 48.86: 20), Se/C@30h (the weight ratios Se : C = 8: 2), P/C@30h (the weight ratios P: C = 8: 2) and C@30h (pure EG), respectively, for the purpose of comparison. It should also be noted that the storage and handling of all samples were performed in glove box (S-IPURE) filled by Argon atmosphere.

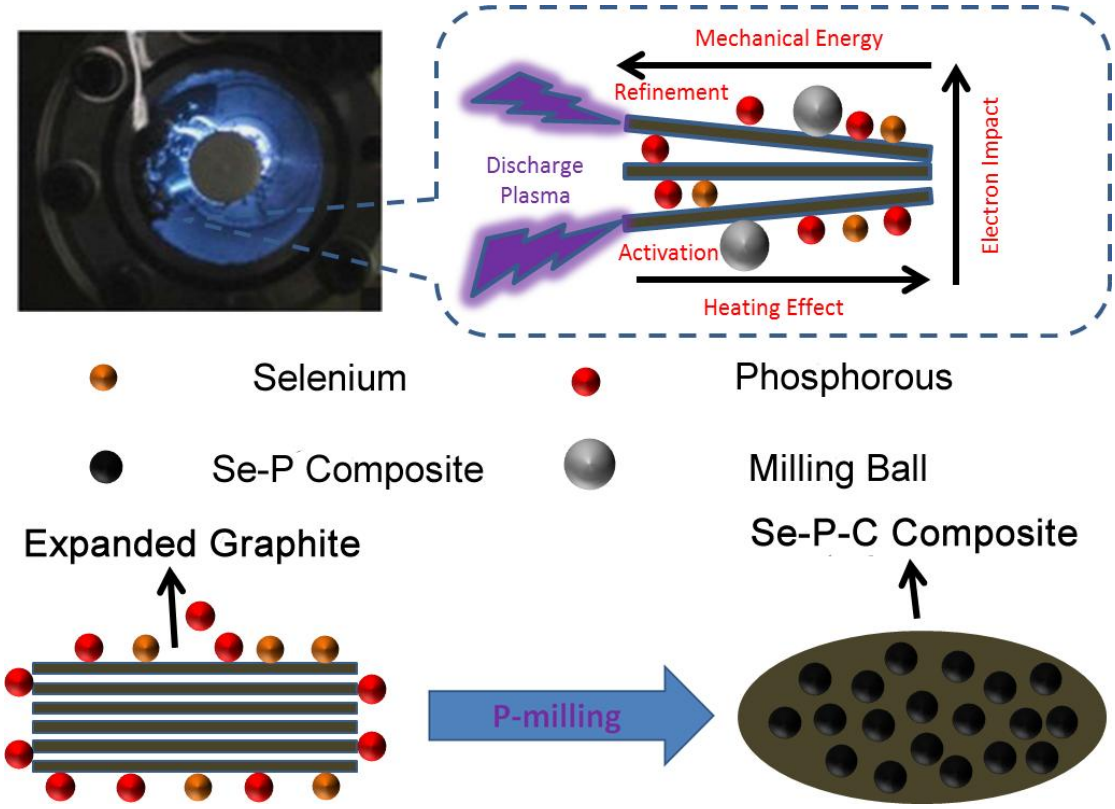

Fig. 1. Schematic illustration of the Se-P-C composite preparation.

2.2 Material characterization

The crystalline structures and phases constitutes of samples were identified by X-ray diffractometry (XRD; Mini Flex 600, Rigaku, Tokyo, Japan) with Cu-*K*α radiation. The morphologies were analyzed by scanning electron microscopy (SEM; Carl Zeiss Supra 40, Baden-Wurttemberg, Oberkochen, Germany). Particularly, more structural details, including interplanar spacing, were further characterized by transmission electron microscopy (TEM; JEOL JEM-2100, Tokyo, Japan) at voltage of 200 kV. The TEM sample preparations were accomplished by dispersing the as-prepared powders on Cu grids before the TEM observations. Raman spectra were obtained on a Jobin-Yvon Labor Raman HR-800 system (Villeneuve d'Ascq, France) with a 514.5

nm Ar-ion laser at 10 mW.

2.3 Electrochemical measurements

Electrochemical performance was tested with a LANHE CT2001A electrochemical workstation (Wuhan. China). The working electrodes were first prepared by mixing the 70 wt.% active material, 20 wt.% Super P carbon black, and 10 wt.% sodium alginate binder to form slurry. The slurry was then pasted on a copper foil and dried at temperature of 60 °C for 12 h in vacuum to form the working electrode. At last, this electrode was punched to the uniform disks with diameter of 12 mm. Each working electrode was then used to construct a 2025 coin-type cell with potassium metal as the counter electrode, 0.8 M potassium hexafluorophosphate (KPF_6) in ethylene carbonate (EC) and diethyl carbonate (DEC) (1:1, v/v) as the electrolyte. Glass fiber membranes (GF/D-125R, Whatman) were used as separators. For comparison, 1 M difluorosulfonimide potassium (KFSI) in 1,2-Dimethoxyethane (DME) was utilized as the electrolyte to assemble the coin cells as well. Galvanostatic charge and discharge tests were carried out in the voltage range 0.01–3 V vs. K^+/K. Cyclic voltammetry (CV) was performed at a scan rate of 0.2 mV s^{-1} using an electrochemical workstation (Gamry, Warminster, PA, USA). The specific capacity was calculated based on the weight of active material. The mass loading of active material was increased to 4 mg cm^{-2} for ex-situ XRD experiments.

3. Result and Discussion

Fig. 2a shows the XRD patterns of the as-prepared Se-2P/C@30h, Se/C@30h and P/C@30h powders, which were synthesized through P-milling process for 30 h, as well as the raw materials of pure Fe, Se and red P. It can be found that the diffraction peaks exhibiting in the XRD pattern of Se-2P/C@30h are quite different from that in the commercial Se and P. In particular, there are three sharp peaks located at 44.58°, 64.8 8°, and 82.14°, respectively, in the XRD pattern of Se-2P/C@30h, Se/C@30h and P/C@30h composites, corresponding to the characteristic peaks of pure Fe. This might be because little pure Fe dropped from the stainless steel vial and stainless steel ball to the composites powder during the high-energy P-milling process. In addition, the XRD patterns of other Se-P-C composites, synthesized with different molar ratios and different ball milling conditions, are given in Fig. S1 (Supporting Information). Fig. 2b displays one SEM image of the as-synthesized Se-2P/C@30h sample which shows the smallest particle size around Se-P-C composite. (Fig. S2 shows the SEM images of all as-synthesized materials). It is clearly seen from Fig. S1a and Fig. 2b that the Se-2P/C@30h powder mainly consists of irregular agglomerated nanometer sized particles. The agglomerated particles consist of many nanoparticles around 10 nm, distributed in the carbon (Fig. 2c). Moreover, high-resolution TEM (HRTEM) image in Fig. 2d indicates that the Se-2P/C@30h nanoparticle has the amorphous structure, which can act as a buffer to relieve the volume changes during the potassiation/depotassiation process [29]. Fig. 2e presents the scanning TEM - energy dispersive spectroscopy (STEM-EDS) elemental mapping analysis of a Se-2P/C@30h particle, indicating the well-distributions of Se, P and C, which proves the sufficient

reaction. Moreover, the EDS analysis demonstrates that the molar ratio of Se/P/C is close to 1:1.88:2.67, being consistent with the designed composition (Experiment Section). From the EDS test (Fig. S3-4, Table S1-3, Supporting Information), it is worth mentioning that Fe contents of the composites prepared by P-milling for 30h stay in the range of 15 ~ 20 wt.%. According to the HRTEM image of Se-2P/C@20h composite in the Fig. S5 (Supporting Information), it can be concluded that the sufficient reaction between Se and P was maintained for the Se-2P/C@30h, which leading to a better electrochemical performance (as evented by the experimental results in the next section). Fig. 2f displays the Raman spectrum of the as-synthesized material, the obscure characteristic peaks for Se-2P/C@30h mainly locate at 320 ~ 390 cm^{-1}, being pretty different from the other as-prepared materials while similar to the Raman-active vibrational modes of the reported Se_4P_4 material [22]. Raman spectrum proves the sufficient reaction between Se and P in Se-2P/C@30h. Meanwhile, more or less Se phase should exist in the Se-2P/C@20h, Se-P/C@30h and Se-4P/C@30h samples because their characteristic peaks locate around 239 – 270 cm^{-1} like Se/C@30h composite. Compared with commercial selenium powder, the Raman characteristic peak of Se phase in Se/C@30h composites is significantly broadened and moved to high wavenumber (blue shift). This phenomenon is caused by a large particle size reduction of Se on the surface of the active material after P-milling process and the TEM analysis in Fig. S6-7 (Supporting Information) proved that there are a large number of filamentous amorphous carbon-coated Se nanocrystal structures on the surface of Se/C@30h composite. Analogously, Se-2P/C@20h,

Se-P/C@30h, Se-4P/C@30h composites also own these similar structures, causing their Raman characteristic peaks of Se showed "blue shift" as well.

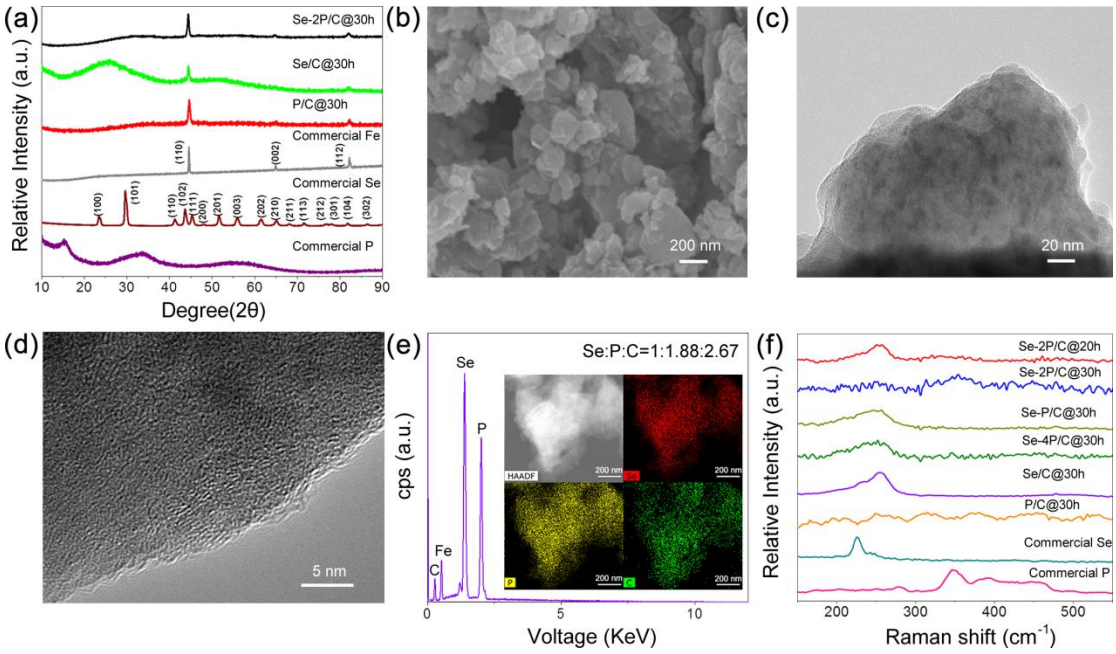

Fig. 2. Characterization of Se-2P/C@30h powder: (a) XRD patterns, (b) SEM image, (c) TEM image, (d) HRTEM image, (e) STEM-EDS and element mappings, (f) Raman spectra.

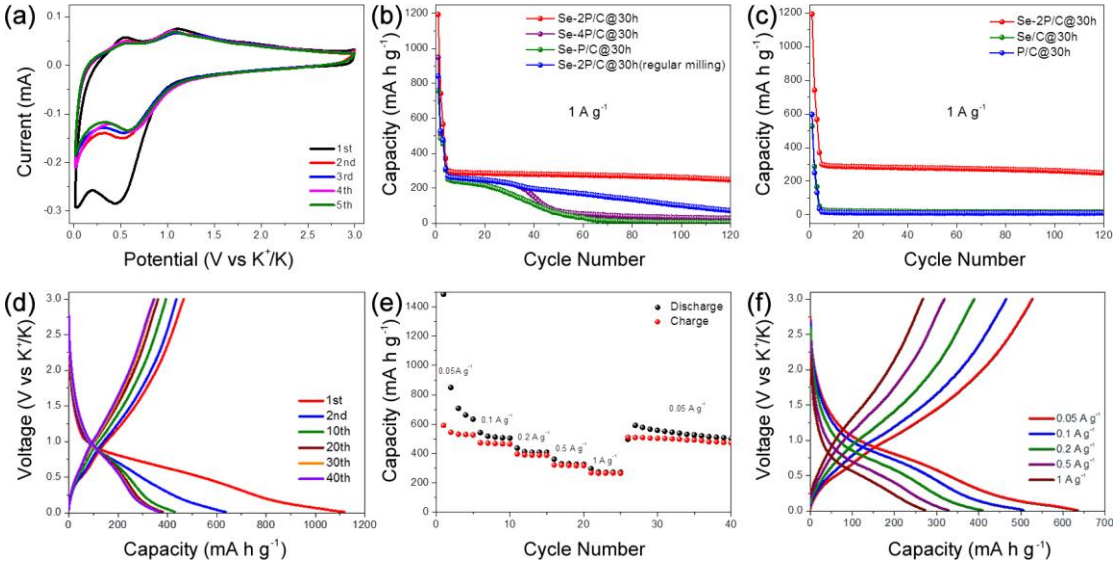

Fig. 3. Electrochemical performance of the Se-2P/C@30h electrode with 0.8 M KPF_6 in EC and DEC as the electrolyte: (a) CV curves with a scan rate of 0.2 mV s^{-1}, (b) comparison of the cycling performance among Se-2P/C@30h, Se-4P/C@30h, Se-P/C@30h and Se-2P/C@30h(regular milling), (c) comparison of the cycling performance among Se-2P/C@30h, Se/C@30h and P/C@30h, (d) galvanostatic discharge and charge curves at the current density of 100 mA h g^{-1}, (e) rate

performance at various current densities, (f) galvanostatic discharge and charge profiles at various current densities.

The electrochemical performance of the as-prepared materials has been investigated by cyclic voltammetry (CV) and galvanostatic discharge/charge techniques. Fig. 3a shows the initial 5 cycles CV profiles of the Se-2P/C@30h at a scan rate of 0.2 mV s^{-1}. There are two reduction bands and two oxidation bands during the first cycle, and then the stable reversible electrochemical behaviors in the subsequent four cycles with normal overlap curves. In detail, two reduction bands (0.44 V and 0.03 V) related to the potassiation reaction locate at cathodic scan curve while 3 oxidation bands (0.55 V, 1.1 V and 1.83 V) caused by the depotassiation process exist in the anodic scan. The reduction peak appearing at 0.03 V and the oxidation peak at 0.55 V respectively correspond to the insertion and extraction of K^+ ions in carbon materials [30]. The reduction peak at 0.44 V and the oxidation peak at 1.1 V are caused by the generation and disappearance of K−P [34]. The disappearance of K−Se contributes to the relatively weak oxidation band at 1.83 V [18]. Fig. 3b shows the cycling performances of the Se-2P/C@30h, Se-4P/C@30h, Se-P/C@30h and Se-2P/C@30h (regular milling) electrodes in PIBs at the current density of 1 A g^{-1}, after an initial three activation cycles at a current density of 100 mA g^{-1}. The discharge capacity of the Se-2P/C@30h electrode (1194 mA h g^{-1}) at the first cycle is higher than those of the Se-4P/C@30h (697 mA hg^{-1}), the Se-P/C@30h (757 mA hg^{-1}) and the Se-2P/C@30h(regular milling) (841 mA h g^{-1}). Although the Se-2P/C@30h material shows the lowest coulombic efficiency of 41.74% at the first cycle (Fig. S8, Supporting Information), it maintains a highest reversible capacity of 248.6 mA h g^{-1}

after 120 cycles at a current density of 1 A g^{-1}, as shown in Fig. 3b-c, which is much better than that of all other electrodes, i.e., Se-4P/C@30h (~29 mA h g^{-1}), Se-P/C@30h(~5 mA h g^{-1}), Se-2P/C@30h(regular milling) (~72 mA h g^{-1}), Se/C@30h (~17 mA h g^{-1}), and P/C@30h(~19 mA h g^{-1}). The amorphous carbon of Se-2P/C@30h delivers a reversible capacity of 125 mA h g^{-1} at the current density of 1 A g^{-1} (Fig. S9, Supporting Information). Se-2P/C@30h anode shows the best electrochemical performance because of its smallest particle size, which shorten the diffusion distance of K^+ ions, and sufficient reaction between Se and P to form Se-P amorphous phase, which not only enhances the conductivity of active material but also avoids the production of polyselenide in discharge/charge process. Fig. 3d displays the galvanostatic discharge/charge curves of the Se-2P/C@30h electrode in the potential range of 0.01 V and 3.0 V at current density of 100 mA g^{-1}. During the first and second cycles, it exhibits the irreversible reaction with low coulombic efficiencies of 41.74% and 68.39%, respectively. However, the coulombic efficiency increases to ~ 95% in the following cycles because of the reversible potassiation/depotassiation process. The long-term cycling performance of Se-2P/C@30h electrode can be seen in the Fig. S10. Moreover, the Se-2P/C@30h electrode demonstrates the outstanding high-rate capacities ranging from 634 mA h g^{-1} at 0.05 A g^{-1} to 272.8 mA h g^{-1} at 1 A g^{-1} (Fig. 3e, f). Interestingly, when the rate is changed back to 0.05 A g^{-1}, the capacity can be recuperated to 592.6 mA h g^{-1}. The electrochemical capability, especially at high current density, can keep pace with the other material for PIBs (Table S4, Supporting Information). According to the

electrochemical impedance spectroscopy in Fig. S11, the charge transfer resistance (Rct) of Se-2P/C@30h electrode is lower than the other composites, indicating that it has better electron transfer capability.

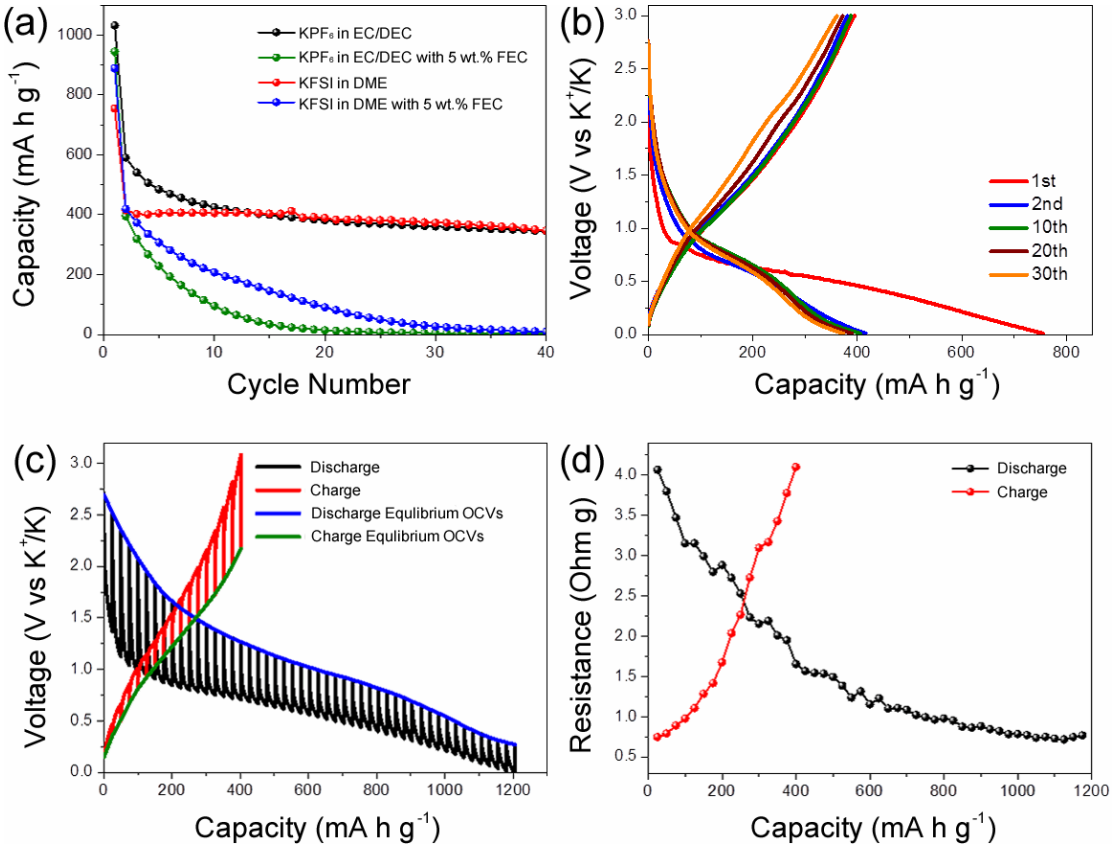

Fig. 4. Electrochemical performance of the Se-2P/C@30h composite electrode: (a) comparison of the cycling performance in different types of electrolyte, (b) galvanostatic discharge and charge curves at the current density of 100 mA h g^{-1} with KFSI in DME as electrolyte, (c) potential response and (d) resistance during GITT measurement.

The KFSI in ethers was used as the electrolyte for potassium battery because it can efficiently passivate the potassium surface and enable reversible potassium plating and stripping electrochemistry [31]. The SEI layer formation caused by the KPF_6 in EC and DEC electrolyte may lead to the initial low coulombic efficiency [32], but the KFSI salt can address this problem and promote a uniform, stable SEI layer which

allows the long cyclability for PIBs [33]. Furthermore, DME-based electrolytes offer a high operational voltage, good rate performance with a negligible solid electrolyte interface, and a small volume expansion [35-36]. To better understand the electrochemical behavior of Se-2P/C@30h electrodes, the cells were tested in four electrolytes at a current density of 100 mA g^{-1}. As shown in Fig. 4a-b, the Se-2P/C@30h electrode with KFSI electrolyte presents a relatively high initial coulombic efficiency of 52.27% (41.74% for KFP_6 in EC and DEC, Fig. S6) and stable cycling performance. With the addition of 5 wt.% FEC to both KPF_6 in EC/DEC and KFSI in DME electrolytes, however, the capacity fades quickly and reaches nearly zero after several cycles. This phenomenon is quite similar to previous research on phosphides, which should be attributed to the addition of FEC that can increase the SEI layer and resistance of charge transfer [32].

The kinetic behavior of potassium storage of the Se-2P/C@30h composite was investigated through galvanostatic intermittent titration technique (GITT). Fig. 4c shows the potential response of Se-2P/C@30h anodes during GITT measurement (running at a current density of 100 mA g^{-1} for 0.25 h and rest for 4 h in each pulse). The detail information of single GITT period is illustrated in the Fig. S12. The overpotential for Se-2P/C@30h anodes in PIBs gradually decreases in the discharge process (potassiation reaction), while increases in the charge process (depotassiation reaction). Fig. 4d shows the resistances of Se-2P/C@-30h anodes at different potassiation/depotassiation levels, which were calculated by dividing the IR drops by the pulse current density. The resistance of the Se-2P/C@30h electrode in the Fig. 4d

performs a gradual decrease with increase of the potassiation level. This result is attributed to the volume expansion during potassiation process that improves the contact between particles, leading to the enhancement of the electrode conductivity. Owing to the volume shrinkage that worsens the contact between active particles, in contrast, the resistance of Se-2P/C@30h anodes increases during the depotassiation process in Fig. 4d.

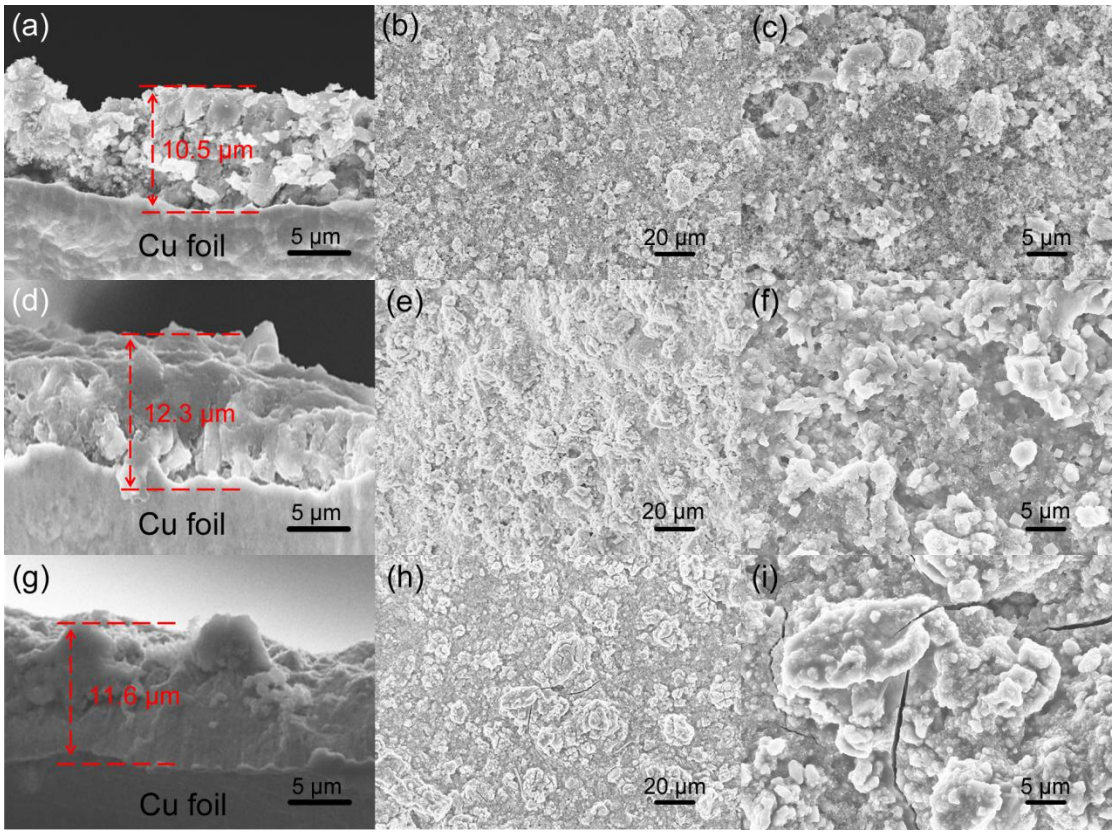

Fig. 5. The SEM images of Se-2P/C@30h composite electrodes: (a-c) fresh electrode, (d-f) potassiation state (discharge to 0.01 V), and (g-i) depotassiation state (charge to 3 V).

The microstructural evolution accompanying with the potassiation/depotassiation processes of Se-2P/C@30h electrode was also investigated to understand the mechanism of volume and structure reversibility. The SME images in Fig. 5 present the thicknesses and surface morphologies of the Se-2P/C@30h electrodes before

potassiation state (a-c), potassiation state (d-f), and depotassiation state (g-i), respectively. The thickness of the Se-2P/C@30h composite electrode increases from 10.5 μm (Fig. 5a) before potassiation state to 12.3 μm (Fig. 5d) after potassiation state and then slightly recover back to 11.6 μm (Fig. 5g) in the depotassiation state. The associated total volume change rate increases ~ 17.14 % during the potassiation process and return to ~ 10.4 % during the depotassiation process. This result shows a quite good volume and structure reversibility of Se-2P/C30h electrodes. Accordingly, it is clearly seen that the size of active particles of Se-2P/C@30h composite electrode grow up from unreacted state (Fig. 5b-c) to potassiation state (Fig. 5e-f), and then slightly reduce to in the depotassiation state, which should be responsible for the volume change existing on the surface during the potassiation/depotassiation process. Meanwhile, few micron-scale cracks are found in Fig. 5i in the Se-2P/C@30h composite electrode after depotassiation process. Furthermore, Fig. S13 displays the obvious capacity fade of Se-2P/C@30h composite electrode after 180 galvanostatic discharge/charge cycles, and correspondingly, Fig. S14 give the SEM images of fresh electrode, the electrode after first potassiation/depotassiation process, and the electrode after 180 potassiation/depotassiation cycles. On one hand, it is worth noted in Fig. S9d-f that micron–crack, which worsens the contact between active particles and material shedding from the electrode, has not grown up obviously after 180 galvanostatic cycles. On the other hand, the growth of active particles of the Se-2P/C@30h electrode can be easily found after 180 discharge/charge cycles. In other words, the growth of active particles in the discharge/charge process causes the

capacity fade of Se-2P/C@30h composite electrode.

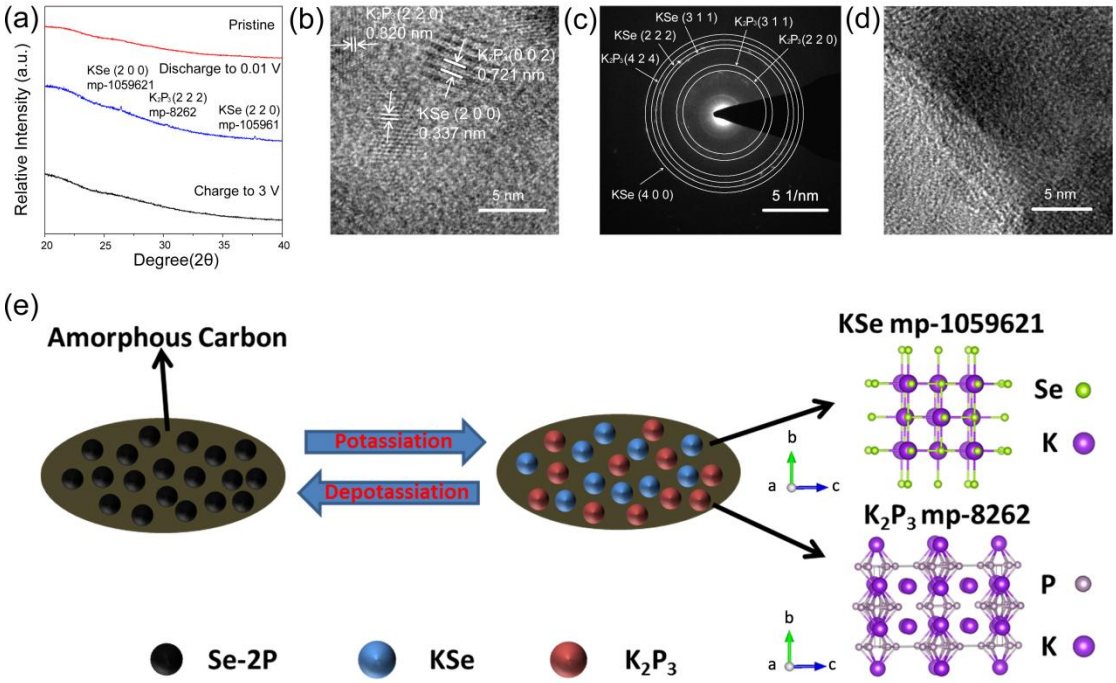

Fig. 6. (a) The ex-situ XRD patterns of Se-2P/C@30h electrodes in pristine, potassiation state (discharge to 0.01 V) and depotassiation state (charge to 3 V). (b) HRTEM image and (c) SAED pattern of Se-2P/C@30h in potassiation state. (d) HRTEM image of Se-2P/C@30h in depotassiation state. (e) A schematic showing the reaction mechanism during potassiation/depotassiation process in Se-2P/C@30h electrode.

Except the Se [18] and red P anode materials [34], the potassium storage mechanism for the Se-P amorphous composite has not yet been investigated. In the present work, first, ex-situ XRD test was utilized to identify the possible phases change during the potassiation and depotassiation process. Fig. 6a shows the ex-situ XRD patterns of Se-2P@30h, electrodes in pristine state, potassiation state (discharge to 0.01 V) and depotassiation state (charge to 3 V). There is no characteristic peak in the pristine amorphous electrode. However, when the electrode is discharged to 0.01 V, the peaks for the KSe (Material ID: mp-1059621) and K_2P_3 ((Material ID: mp-8262) phases could be detected. The details for the characteristic peaks, structural parameters, and

atomic position and the calculating powder diffraction parameters of KSe and K_2P_3 phases are provided in the Fig. S15-18 and Table S5-7 (Supporting Information). , No characteristic peaks for KSe and K_2P_3 phases could be detected in the XRD pattern of the Se-2P@30h electrode once turned back to the depotassiation state.

In addition, the HRTEM observations were further performed to dissect the potassiation storage mechanism for Se-2P/C@30h amorphous composite. Different from the amorphous structure (Fig. 2d) in pristine Se-2P/C@30h,the new phases with nanocrystalline structures appear in the potassiation state, as indicate in Fig. 6b. In particular, the lattice spacing of one phase is indexed as 0.337 nm, corresponding to the (200) plane of cubic phase of KSe; while another one with the lattice spacings of 0.320 and 0.721 nm, can be respectively indexed to the (220) and (002) planes of an orthorhombic phase of K_2P_3. Besides, the corresponding SAED pattern (Fig. 6c) can be indexed to the (311), (222) and (400) planes of KSe and the (220), (311) and (424) planes of K_2P_3. When the Se-2P/C@30h electrode is returned back to the depotassiation state, nanocrystalline structural KSe and K_2P_3 phases disappear and the original amorphous structure appears again (Fig. 6d). The results of ex-XRD measurement together with HRTEM observations reveal that Se-2P/C@30h material undergo the reversible potassiation/depotassiation reaction in the discharge/charge process. More specifically, the corresponding potassiation and depotassiation mechanism for Se-2P/C@30h material can be described by the following equation:

$$3(\text{Se-2P}) + 7K \leftrightarrow 3KSe + 2K_2P_3 \quad (1)$$

For the first time, the Se-2P/C material is tested as an anode for PIBs in the present work. Accordingly, the reaction mechanisms of Se-2P/C@30h anode material with the formation of KSe and K_2P_3 phases are little different from the $K_{2-x}Se$ [18] and $K_{3-x}P$ [20, 21, 32, 34] phases that formed in previous anodes (Se, P, and Sn_4P_3) for PIBs and Se_4P_4 anode for SIBs. However, the potassiation process accompanied with the KSe and K_2P_3 phases is incompletely accomplished, so the practical capacity (634 mA h g^{-1}, 50 mA g^{-1}) in the present work is lower than the theoretical capacities of pure Se (675 mA h g^{-1}) and pure P (2596 mA h g^{-1}). Fig. S19-21 display the EDS maps of the Se-2P/C@30h electrodes in the first potassiation state, depotassiation state and depotassiation state after 150th cycles, respectively. In the first potassiation state (Fig. S19), the Se-2P/C@30h electrode is uniformly distributed by K, Se, P and C. In the first depotassiation state (Fig. S20, Supporting Information), it is found that the signals of Se and P elements are overlapped at the same areas, indicating the reversible potassiation and depotassiation reaction for the potassium storage of Se-2P/C@30h electrode. Besides, some other signals for P element, which may be indexed to the formation of SEI film in the discharge process, exist on the other section and overlap with carbon element. After the depotassiation state of 150th cycle (Fig. S21), the particles of Se-2P/C@30h material are obvious larger than those in the first depotassiation state. This result is in accordance with the SEM images (Fig. 5h-i) and indicates the particles growth in the discharge and charge process.

4. Conclusion

For the first time, the Se-P amorphous composites were prepared by P-milling-method and tested as an anode for PIB in the present work. When the molar ratio of Se to P is 1:2 and the ideal P-milling time is 30 h, the corresponding Se-2P/C@30h amorphous composite anode shows the best electrochemical performance. It is attributed to the smallest particle size, which shorten the diffusion distance of K^+ ions, and sufficient reaction between Se and P to form Se-P amorphous phase which not only enhances the conductivity of active material but also avoids the production of polyselenide in discharge/charge process. As a result, the Se-2P/C@30h composite delivers a high reversible capacity (634 mA h g^{-1} at 0.05 A g^{-1}) and cycling stability (248.6 mA h g^{-1} at 1 A g^{-1} after 120 cycles). The gradually growth of the active particles should be responsible for the capacity fade of the electrode, leading to the loss of nanoparticles function. Moreover, the reaction mechanisms of the Se-2P/C have been revealed as the formation of new K−P (K_2P_3) and K−Se (KSe) phases during the potassiation process. Besides, it should be mentioned that the potassiation process accompanied with the KSe and K_2P_3 phases is incompletely accomplished, since the practical capacity (634 mA h g^{-1}, 50 mA g^{-1}) in the present work is lower than the theoretical capacities of pure Se (675 mA h g^{-1}) and pure P (2596 mA h g^{-1}). The findings in the present work may help in the development of a safe and high-energy-density, rechargeable K-ion battery for the large-scale energy storage applications.

Acknowledgement

This work was supported by the Foundation for Innovative Research Groups of the National Natural Science Foundation of China (No. NSFC51621001), National Natural Science Foundation of China Projects (Nos. 51771075 and 51701171) and by the Project Supported by Natural Science Foundation of Guangdong Province of China (No. 2016A030312011). Author Ouyang also thanks Guangdong Province Universities and Colleges Pearl River Scholar Funded Scheme (2014).

References

[1] A. F. Hollemann and N. Wiberg, Lehrbuch der Anorganischen Chemie, de Gruyter, Berlin, 2007.

[2] A.P. Cohn, K. Share, R. Carter, L. Oakes, C.L. Pint, Ultrafast Solvent-Assisted Sodium Ion Intercalation into Highly Crystalline Few-Layered Graphene, Nano Lett. 16 (2016) 543–548.

[3] X. Xu, J. Liu, Z. Liu, J. Shen, R.Hu, J. Liu, L. Ouyang, L. Zhang, M. Zhu, Robust Pitaya-Structured Pyrite as High Energy Density Cathode for High-Rate Lithium Batteries, Acs Nano 11(2017) 9033-9040.

[4] Z. Jian, Z. Xing, C. Bommier, Z. Li, X. Ji, Hard Carbon Microspheres: Potassium‐Ion Anode Versus Sodium‐Ion Anode, Adv. Energy Mater., 6(2016) 1501874

[5] M. Lin, M. Gong, B. Lu, Y. Wu, D. Wang, M. Guan, M. Angell, C. Chen, J. Yang, B. Hwang, H. Dai, An ultrafast rechargeable aluminium-ion battery, Nature 520.7547(2015) 325-328.

[6] H. Yoo, I. Shterenberg, Y. Gofer, G. Gershinsky, N. Pour, D. Aurbach, Mg rechargeable batteries: an on-going challenge, Energ. Environ. Sci. 6.8(2013) 2265-2279.

[7] K. A. See, J. A. Gerbec , Y. Jun , F. Wudl , G. D. Stucky, R. Seshadri, A High Capacity Calcium Primary Cell Based on the Ca–S System, Adv. Energy Mater. 3.8(2013) 1056-1061.

[8] H.S. Kim, T.S. Arthur, G.D. Allred, J. Zajicek, J.G. Newman, A.E. Rodnyansky, A.G. Oliver, W.C. Boggess, J. Muldoon, Structure and compatibility of a magnesium electrolyte with a sulphur cathode, Nat. Commun. 2(2011) 427.

[9] R.C. Asher, S. A. Wilson., Lamellar Compound of Sodium with Graphite, Nature 181.4606(1958) 409-410.

[10] P. Ge, M. Fouletier, Electrochemical intercalation of sodium in graphite, Solid State Ionics, 28(1988) 1172-1175.

[11] Z. Jian, W. Luo, X. Ji, Carbon Electrodes for K-Ion Batteries, J. Am. Chem. Soc. 137.36(2015) 11566.

[12] S. Komaba S, T. Hasegawa T, M. Dahbi M, K. Kei, Potassium intercalation into graphite to realize high-voltage/high-power potassium-ion batteries and potassium-ion capacitors, Electrochem. Commun. 60(2015) 172-175.

[13] Y. Liu, F. Fan, J. Wang, Y. Liu, H. Chen, K.Y. Jungjohann, Y. Xu, Y. Zhu, D. Bigio, T. Zhu, C. Wang, In situ transmission electron microscopy study of electrochemical sodiation and potassiation of carbon nanofibers, Nano Lett. 14.6(2014) 3445-3452.

[14] Z. Jian, Z. Xing, C. Bommier, Z. Li, X. Ji, Anode Materials: Hard Carbon Microspheres: Potassium on Anode Versus Sodium on Anode , Adv. Energy Mater. 6.3(2016) 1501874.

[15] K. Share, A. P. Cohn, R. Carter, B. Rogers, C. L. Pint, Role of Nitrogen Doped Graphene for Improved High Capacity Potassium Ion Battery Anodes, Acs Nano 10.10(2016) 9738-9744.

[16] Z. Jian, W. Luo, X. Ji, Carbon electrodes for K-ion batteries, J. Am. Chem. Soc. 137.36(2015) 11566-11569.

[17] Q. Zhao, Y. Hu, K. Zhang, J. Chen, Potassium–sulfur batteries: A new member of room-temperature rechargeable metal–sulfur batteries, Inorg. Chem. 53.17(2014) 9000-9005.

[18] Liu Y, Tai Z, Zhang Q, et al. Y. Liu, Z. Tai, Q. Zhang, H. Wang, W. Pang, H Liu, K. Konstantinova, Z. Guo, A new energy storage system: Rechargeable potassium-selenium battery, Nano Energy, 35(2017) 36-43.

[19] I. Sultana, T. Ramireddy, M. M. Rahman, Y. Chen, A. M. Glushenkov, Tin-based composite anodes for potassium-ion batteries, Chem. Commun. 52.59(2016) 9279-9282.

[20] I. Sultana, M. M. Rahman, T. Ramireddy, Y. Chen, A. M. Glushenkov, High capacity potassium-ion battery anodes based on black phosphorus, J. Mater. Chem. A 5.45(2017) 23506-23512.

[21] W. Zhang, J. Mao, S. Li, Z. Chen, Z. Guo, Phosphorus-based alloy materials for advanced potassium-ion battery anode, J. Am. Chem. Soc. 139.9(2017) 3316-3319.

[22] Y. Lu, P. Zhou, K. Lei, Q. Zhao, Z. Tao, J. Chen, Selenium Phosphide (Se_4P_4) as a New and Promising Anode Material for Sodium‐Ion Batteries, Adv. Energy Mater. 7.7(2017) 1601973.

[23] A. Bytchkov, M. Miloshova, E. Bychkov, S. Kohara, L. Hennet, D. L. Price, Intermediate-and short-range order in phosphorus-selenium glasses, Phys. Rev. B 83.14(2011) 144201.

[24] L. Ouyang, Z. Cao, H. Wang, R. Hu, M. Zhu, Application of Dielectric Barrier Discharge Plasma–assisted Milling in Energy Storage Materials – A review, J. Alloys Compd. 691 (2017) 422-435.

[25] L. Ouyang, L. Guo, W. Cai, J. Ye, R. Hu, L. Yang, M. Zhu, Facile Synthesis of Ge@FLG Composites by Plasma Assisted Ball Milling for Lithium Ion Battery Anodes, J. Mater. Chem. A 2(2014) 11280-11285.

[26] C. Lin, L. Yang, L. Ouyang, J. Liu, H. Wang, M. Zhu, A new method for few-layer graphene preparation via plasma-assisted ball milling, J. Alloys Compd. 728(2017) 578-584.

[27] L. Dai, B. Cao, M. Zhu, Comparison on refinement of iron powder by ball milling assisted by different external fields, Acta Metall. Sin.-Engl 19.6(2006) 411-417, http://dx.doi.org/10.1016/S1006-7191(06)62081-4.

[28] M. Zhu, L. Dai, N. Gu, B. Cao, L. Ouyang, Synergism of mechanical milling and dielectric barrier discharge plasma on the fabrication of nano-powders of pure metals and tungsten carbide, J. Alloys Compd 478.1(2009) 624-629, http://dx.doi.org/10.1016/j.jallcom.2008.11.122.

[29] L. Lin, X. Xu, C. Chu, M. K. Majeed, J. Yang, Mesoporous Amorphous Silicon: A Simple Synthesis of a High-Rate and Long-Life Anode Material for Lithium-Ion Batteries, Angew. Chem. Int. Edit. 55.45(2016) 14063-14066.

[30] N. Xiao, W. D. McCulloch, Y. Wu, Reversible dendrite-free potassium plating and stripping electrochemistry for potassium secondary batteries, J. Am. Chem. Soc. 139.28(2017) 9475-9478.

[31] X. Zhao, P. Xiong, J. Meng, Y. Liang, J. Wang, Y. Xu, High rate and long cycle life porous carbon nanofiber paper anodes for potassium-ion batteries, J. Mater. Chem. A 5(2017) 19237-19244. http://dx.doi.org/10.1039/C7TA04264G

[32] W. Zhang, W. Pang, V. Sencadas, Z. Guo, Understanding High-Energy-Density Sn_4P_3 Anodes for Potassium-Ion Batteries, Joule 2.8 (2018) 1534-1547.

[33] W. Zhang, Z. Wu, J. Zhang, G. Liu, N. Yang, R. Liu, R. Liu, W. Pang, W. Li, Z. Guo, Unraveling the effect of salt chemistry on long-durability high-phosphorus-concentration anode for potassium ion batteries, Nano Energy 53(2018) 967-974.

[34] P. Xiong, P. Bai, S. Tu, M. Cheng, J. Zhang, J. Sun, Y. Xu, Red Phosphorus Nanoparticle@3D Interconnected Carbon Nanosheet Framework Composite for Potassium-Ion Battery Anodes, Small 14.33(2018) 1802140.

[35] L. Wang, J. Yang, J. Li, T. Chen, S. Chen, Z. Wu, J. Qiu, B. Wang, P. Gao, X. Niu, H. Li, Graphite as a potassium ion battery anode in carbonate-based electrolyte and ether-based electrolyte, J. Power Sources 409(2019) 24-30.

[36] L. Wang, J. Zou, S. Chen, G. Zhou, J. Bai, P. Gao, Y. Wang, X. Yu, J. Li, Y. Hu, H. Li, TiS_2 as a high performance potassium ion battery cathode in ether-based electrolyte, Energy Storage Mater. 12(2018) 216-222.

A novel Selenium-Phosphorous amorphous Composite by Plasma Assisted Ball Milling for high-performance Rechargeable Potassium-Ion Battery Anode

Cheng Lin[a], Liuzhang Ouyang[a,b,c]*, Chaojin Zhou[a], Renzong Hu[a,b], Lichun Yang[a], Xusheng Yang[c,d]*, Huaiyu Shao[e], Min Zhu[a,b]

[a]*School of Materials Science and Engineering, Guangdong Provincial Key Laboratory of Advanced Energy Storage Materials, South China University of Technology, Guangzhou, 510641, People's Republic of China*

[b]*China-Australia Joint Laboratory for Energy & Environmental Materials, Key Laboratory of Fuel Cell Technology of Guangdong Province, Guangzhou, Guangzhou, 510641, People's Republic of China*

[c]*Department of Industrial and Systems Engineering, The Hong Kong Polytechnic University, Hung Hom, Kowloon, Hong Kong, China*

[d]*Hong Kong Polytechnic University Shenzhen Research Institute, Shenzhen 518057, China*

[e]*Joint Key Laboratory of the Ministry of Education, Institute of Applied Physics and Materials Engineering (IAPME), University of Macau, Taipa, Macau SAR, China*

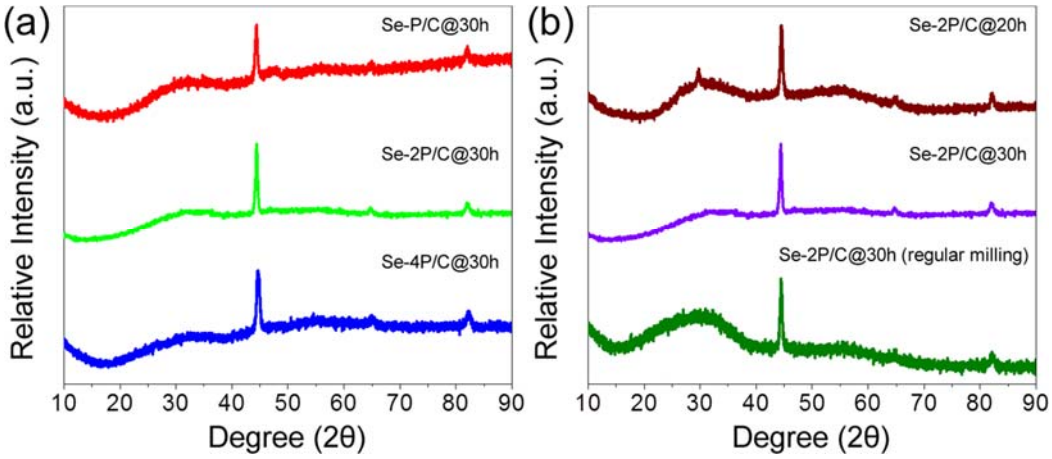

Fig. S1. (a) XRD patterns of the Se-P-C composites with different molar ratios. (b) XRD patterns of the Se-P-C composites under different ball milling conditions.

In Fig. S1a, it can be known that the samples (molar ratio of Se: P = 1:1, 1:2 and 1:4 respectively) after 30 hours P-milling process show the peaks at 44.58°, 64.88° and 82.14°, which are referred to the commercial Fe in Fig. 1a. It indicates that the sufficient reaction between Se and P. The XRD patterns of Se-2P/C composites prepared under different ball milling conditions (P-milling for 20 hours, P-milling for 30 hours and milling for 30 hours) are shown in the Fig. S1b. Unlike the samples which were prepared by P-milling and milling for 30 hours, a small peak at the 29.70° can be found in the pattern of Se-2P/C@20h sample and it can attribute to raw

material.

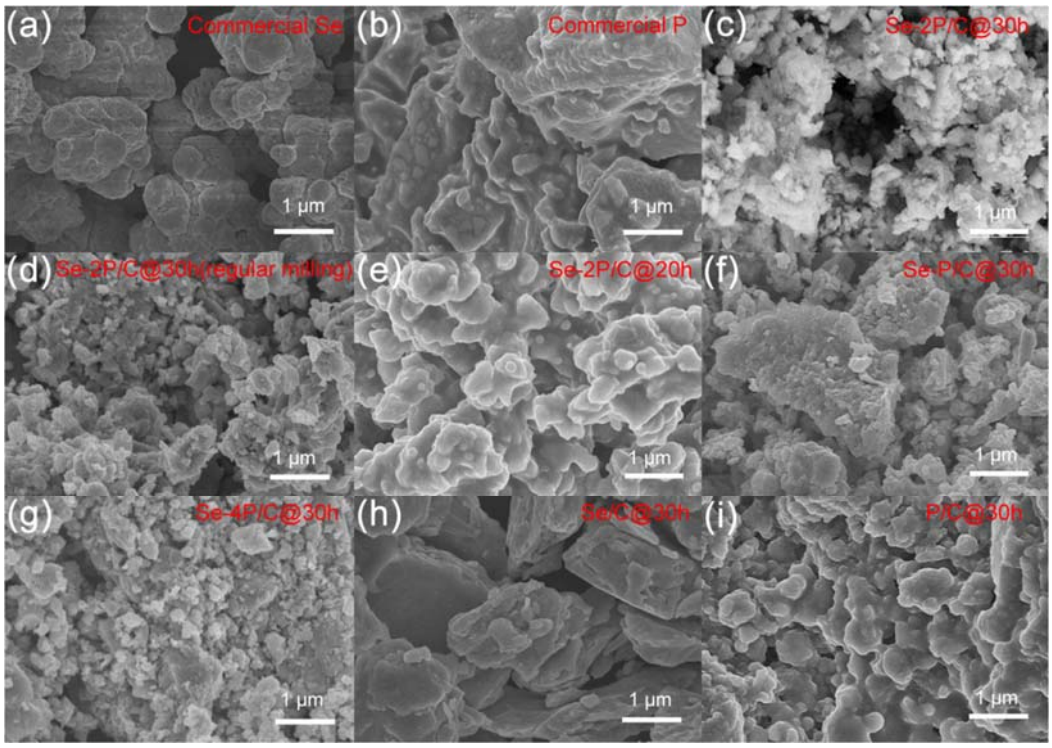

Fig. S2. SEM images of (a) commercial selenium powder, (b) commercial red phosphorous, (c) Se-2P/C@30h, (d) Se-2P/C@30h(regular milling), (e) Se-2P/C@20h, (f) Se-P/C@30h, (g) Se-4P/C@30h, (h) Se/C@30h and (i) P/C@30h.

According to the Fig. S2a-b, the commercial selenium powder and red phosphorus without milling process have large particle with micron size. It can be found in Fig. S2c-d that the particle sizes of Se-2P/C@30h and Se-2P/C@30h(regular milling) composites decreased to nanometer size through ball-milling treatment. Since P-milling method provides more energy than ordinary ball milling, the size of the particles without significant agglomeration of Se-2P/C@30h (30-40 nm) is lower than that of Se-2P/C@30h(regular milling) (50-70 nm). It can be observed from Fig. S2e that the particles size of Se-2P/C@20h is substantially on the order of micrometers, indicating that the 20-hour P-milling process did not decrease particle size of Se-2P/C

into nano-scale. In Fig. S2f, it can be seen that Se-P/C@30h composite contains more micron-sized particles, and the average size of small particles which did not significantly agglomerated is 80-60 nm. Se-4P/C@30h composite in Fig. S2g shows overall lower particle size and the average size of small particles which did not significantly agglomerated is only 40-60 nm. In the same P-milling time of 30 h, Se/C@30h (Fig. S2h) and P/C@30h (Fig. S2i) composites show larger particle size than the other as-prepared composites. Moreover, Se is proved more difficult to reduce its particle size in P-milling process than Red phosphorous as Se/C@30h shows huger particle size. The similar situation also occurs in the P-milling process of Se powder, red phosphorus and expanded graphite. The particle size of Se-P/C@30h composite with higher Se content is significantly larger than those of Se-2P/C@30h and Se-4P/C@30h composites.

Table. S1. Element content of Se-2P/C@30h.

Element	Mass Ratio (%)	Atom Ratio (%)
Se	39.04	15.39
P	26.68	26.81
C	19.04	49.32
Fe	15.24	8.49

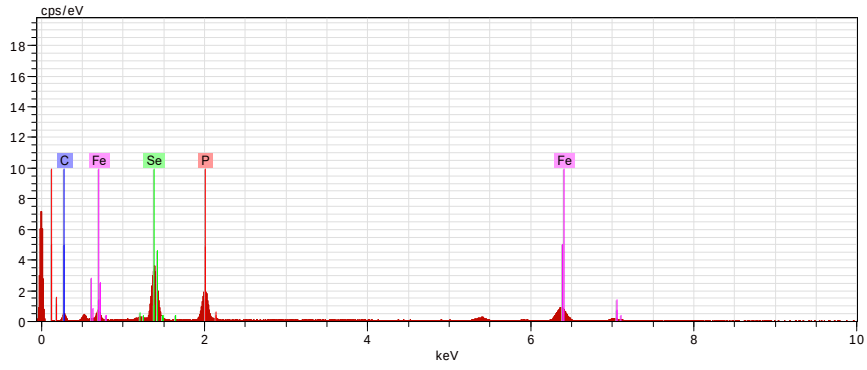

Fig. S3 EDS of Se-P/C@30h.

Table. S2. Element content of Se-P/C@30h.

Element	Mass Ratio (%)	Atom Ratio (%)
Se	45.77	19.15
P	18.85	20.12
C	18.41	50.71
Fe	16.96	10.01

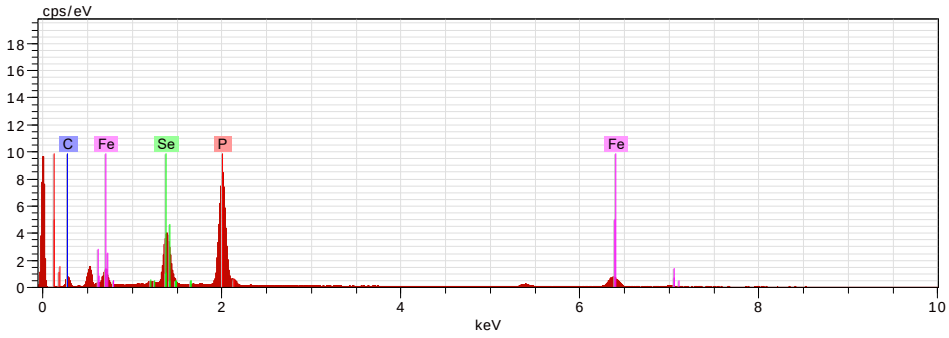

Fig. S4 EDS of Se-4P/C@30h.

Table. S3. Element content of Se-4P/C@30h.

Element	Mass Ratio (%)	Atom Ratio (%)
Se	22.44	7.70
P	34.51	30.19
C	23.28	52.55
Fe	19.76	9.56

The Fe content of Se-2P/C@30h, Se-P/C@30h and Se-4P/C@30h are shown in Table S1-3, respectively. From these tables, it is known that the Fe content of Se-2P/C@30h, Se-P/C@30h and Se-4P/C@30h are 15.24 wt.%, 16.96 wt.% and 19.76 wt.%, respectively. As the Fe contents of the samples stay in the range of 15 ~ 20%, the influence factors for Se-P-C composites on potassium storage should be the particle size and the combination level of Se and P, instead of Fe content.

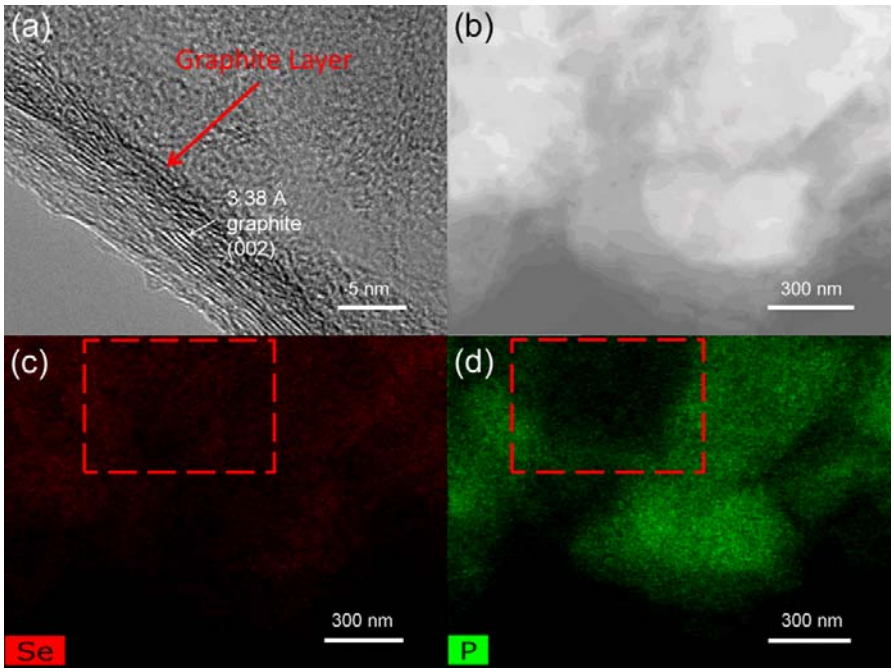

Fig. S5. Characterization of Se-2P/C@20h powder: (a) HRTEM image, (b-d) element mappings.

Graphite layer can be found in Fig. S5a, indicating that the carbon morphology of Se-2P/C@20h is quite different from the amorphous carbon of Se-2P/C@30h in Fig. 2d. In addition, unlike the material prepared by P-milling method for 30 h (Fig. 2e), the red outlines in the Fig. S3b-d indicate that the insufficient reaction between Se and P.

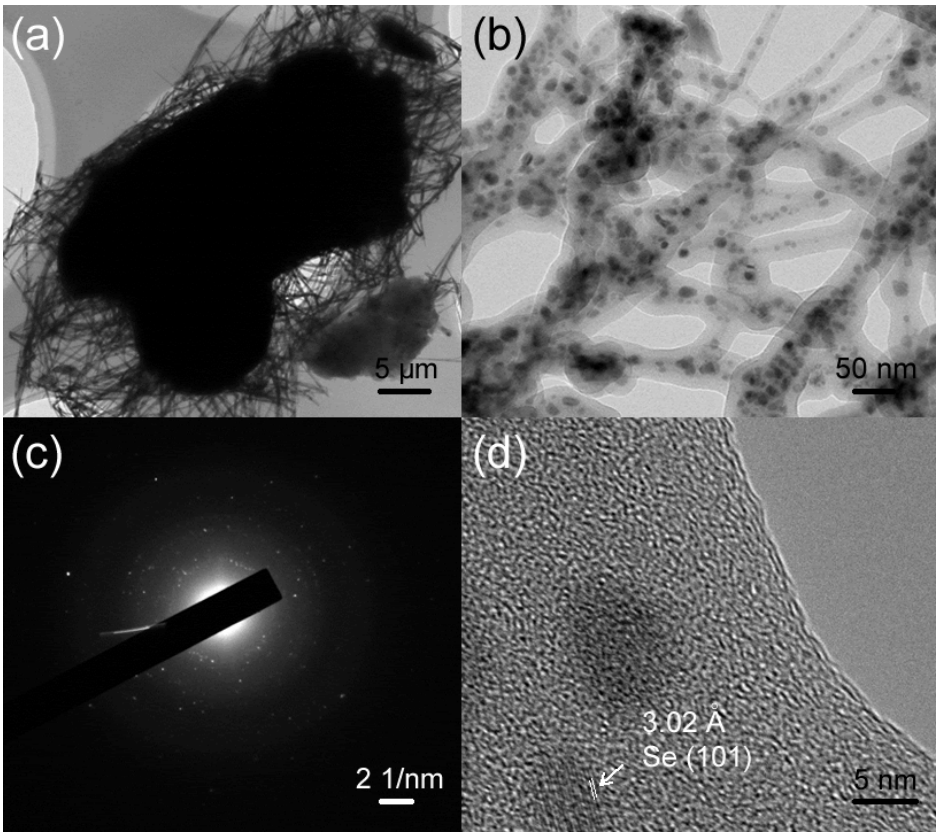

Fig. S6. (a) STEM image, (b) TEM image, (c) SAED pattern and (d) HRTEM image of Se/C@30h composite.

Fig. S6a shows the STEM image of the Se/C@30h composite. It can be observed that a lot of filamentous substances appear on the surface of a large bulk. According to the TEM image (Fig. S6b), it is found that there are many small particles (3-10 nm) inside the filamentous substance, indicating that the Se nanoparticles (the darker portion) are surrounded by the filamentous carbon matrix (the brighter portion). Fig. S6c displays the SAED image of the filamentous substance. Many weak irregular diffraction spots and a diffraction ring can also be observed in the Fig. S6c, indicating the presence of single crystal and amorphous structures inside the filamentous substance. It can be seen from Fig. S6d (HRTEM image of filamentous substances of

Se/C@30h composite) that the lattice spacing of the darker nanoparticles is 3.02 Å which corresponds with the lattice distance of the Se (101) crystal plane, further demonstrating that Se single crystals exist inside the filamentous substances.

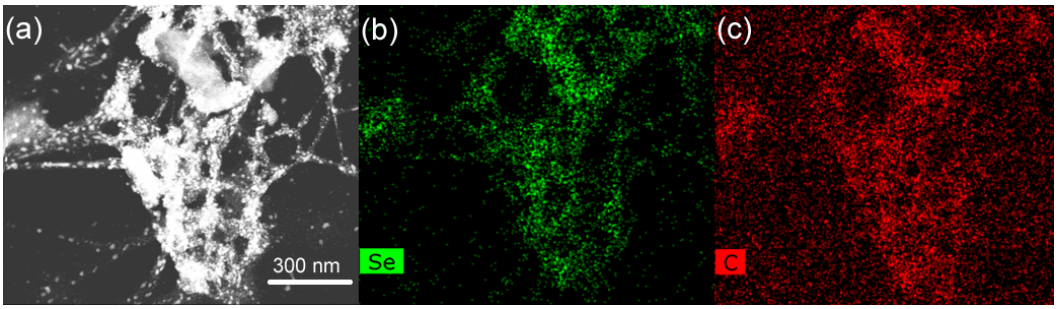

Fig. S7 (a) STEM image and (b-c) Element mapping image of Se/C@30h composite.

Fig. S7a and S7b-c display STEM image and element mapping images of Se/C@30h, respectively. According to Fig. S7, it is found that the elemental signals of Se and C not only coincide with each other but also substantially accord with the filamentous substance, further demonstrating that the filamentous substance consist of Se and C.

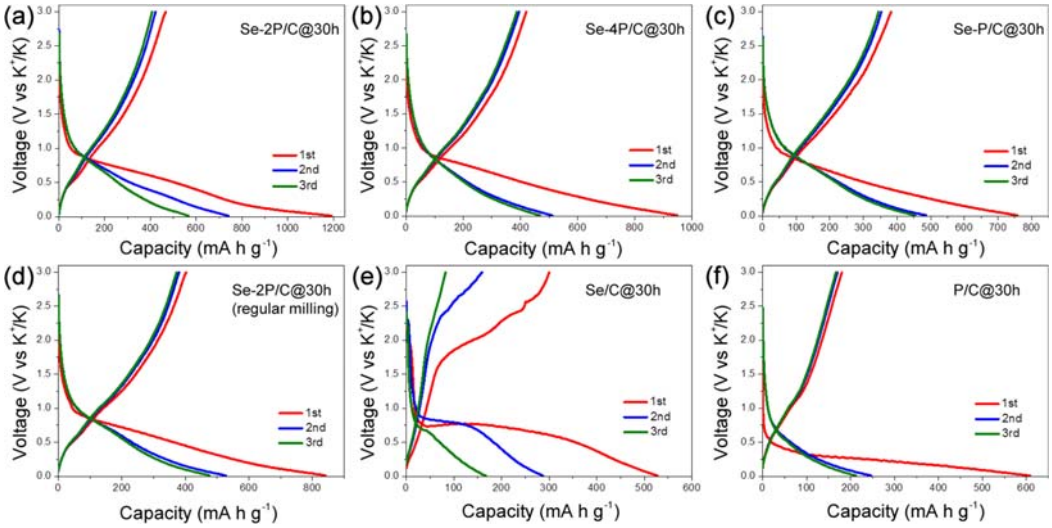

Fig. S8. Discharge/charge profiles for the first 3 cycles of (a) Se-2P/C@30h, (b) Se-4P/C @30h, (c) Se-P/C@30h, (d) Se-2P/C@30h(regular milling), (e) Se/C-@30h, (f) P/C @30h.

It is clearly known that the first coulombic efficiencies for the materials Se-2P/C@30h, Se-4P/C@30h, Se-P/C@30h, Se-2P/C@30h(regular milling), Se/C@30h and P/C@30h are 41.74%, 42.69%, 50.48%, 47.48%, 56.92% and 29.64% respectively.

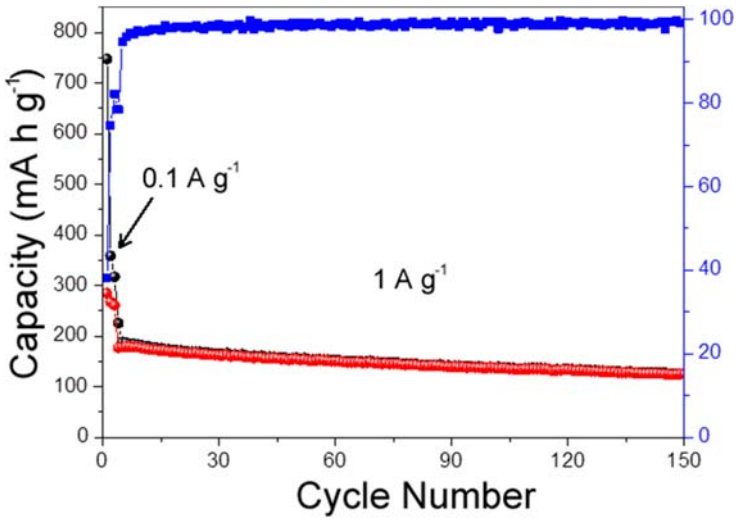

Fig. S9. Cycling performance of the C@30h electrode in PIBs at a current density of 1 A g^{-1}.

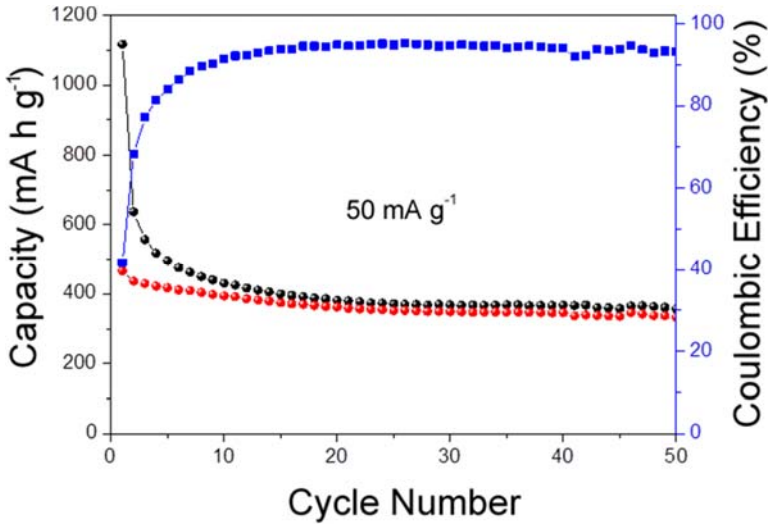

Fig. S10. Long-term cycling performance of the Se-2P/C@30h electrode in PIBs at a current density of 50 mA g^{-1}.

Table S4. The potassium storage performances of Se-2P/C@30h and other anode materials.

Sample	Capacity	Current Density	Reference
Se-2P/C@30h	248.6 mA h g^{-1}	1 A g^{-1}	This work
GeP_5	230 mA h g^{-1}	1 A g^{-1}	[1]
Sn_4P_3@carbon fiber	233.8 mA h g^{-1}	1 A g^{-1}	[2]
Sn_4P_3	221.9 mA h g^{-1}	1 A g^{-1}	[3]
Sn/C	150 mA h g^{-1}	25 mA g^{-1}	[4]
3D Sn/C	150 mA h g^{-1}	500 mA g^{-1}	[5]
Bi/rGO	235 mA h g^{-1}	500 mA g^{-1}	[6]
MoS_2	65 mA h g^{-1}	20 mA g^{-1}	[7]

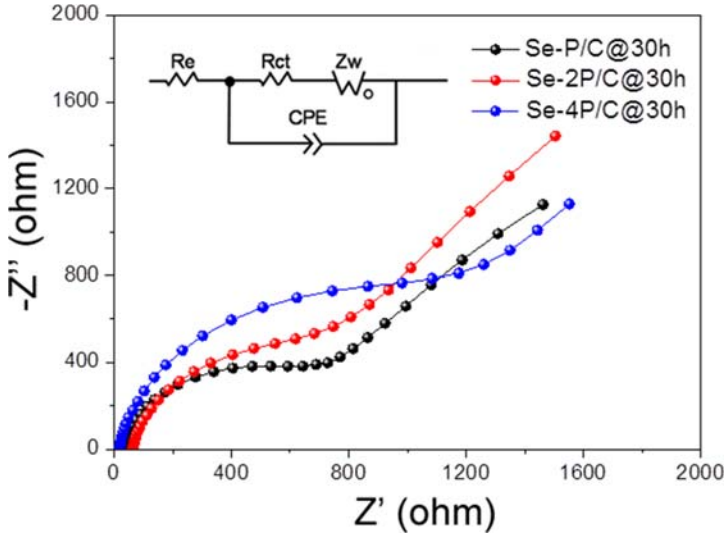

Fig. S11. Nyquist plots of Se-P/C@30h, Se-2P/C@30h and Se-4P/C@30h electrodes after first cycle in potassium ion batteries (the inset figure is corresponding to equivalent circuit).

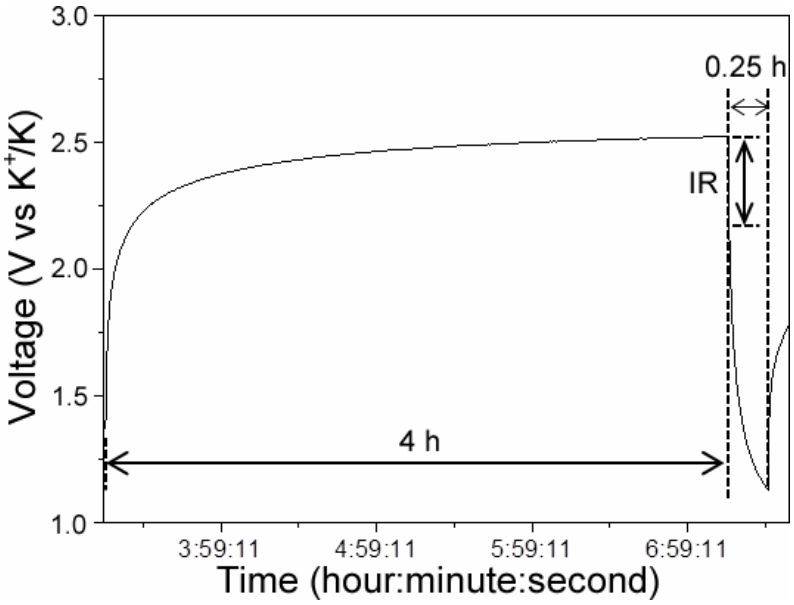

Fig. S12. Voltage-Time diagram for the Se-2P/C@30h electrode on potassium storage in the GITT process.

According to Fig. S12, when the cell started from rest to discharge, instantaneous

voltage drop happened and this instantaneous voltage drop should be IR drop. In the case of calculating resistances, the IR drops were divided by the pulse current density (100 mA g^{-1}) and the resistances could be achieved.

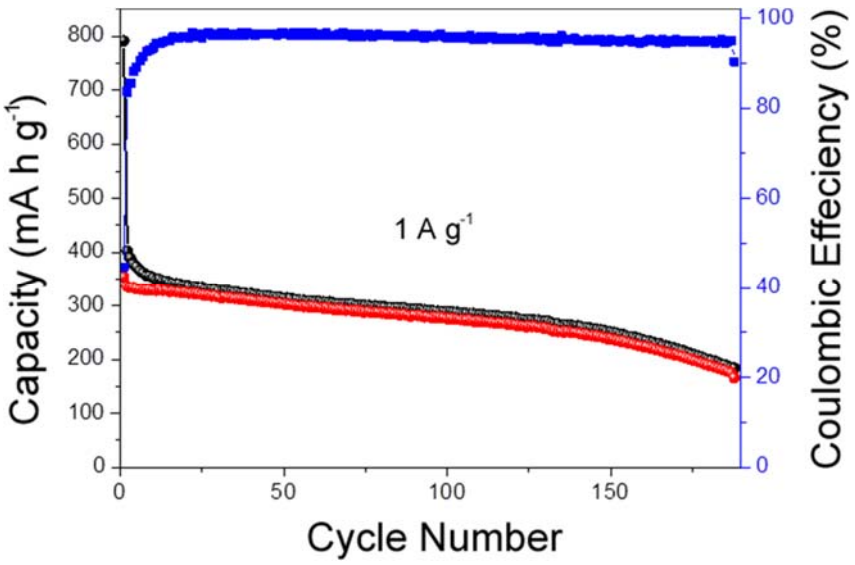

Fig. S13. Long-term cycling performance of the Se-2P/C@30h electrode in PIBs at a current density of 1 A g^{-1}.

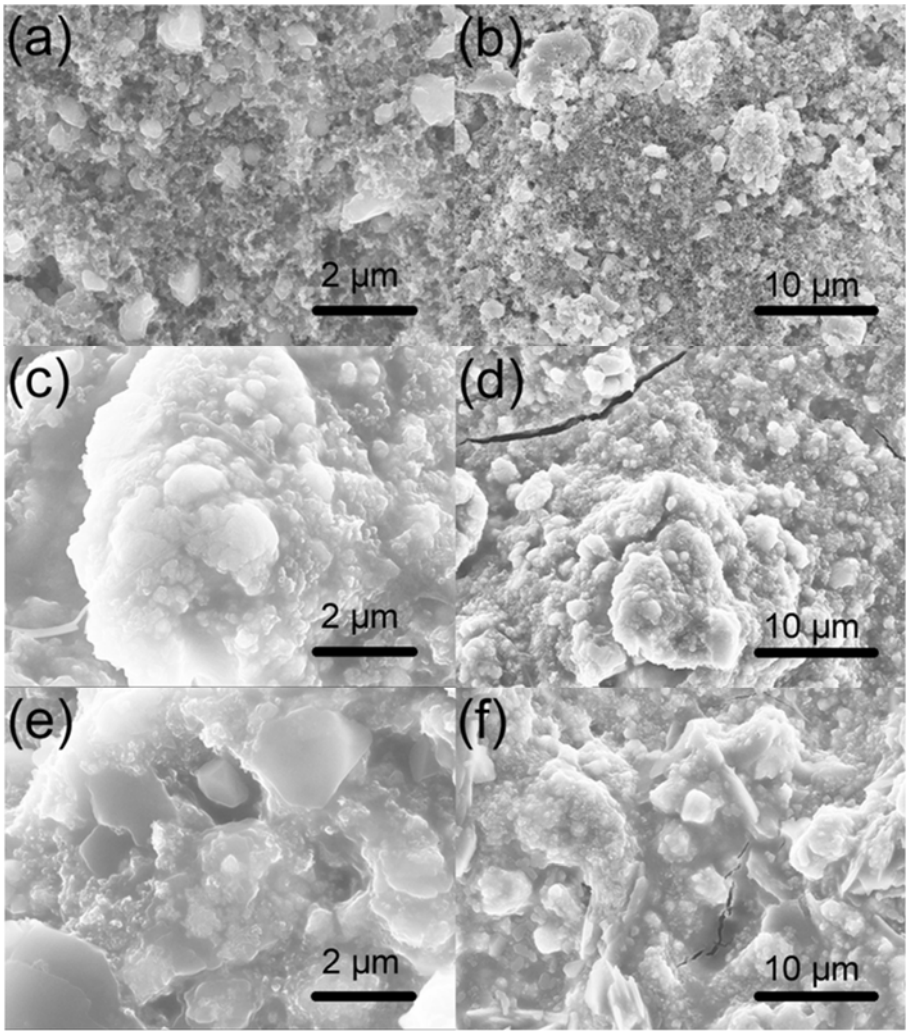

Fig. S14. The SEM images of Se-2P/C@30h electrodes: (a-b) fresh electrode, (c-d) the electrode after first potassiation/depotassiation process, (e-f) the electrode after 180 potassiation/depotassiation cycles.

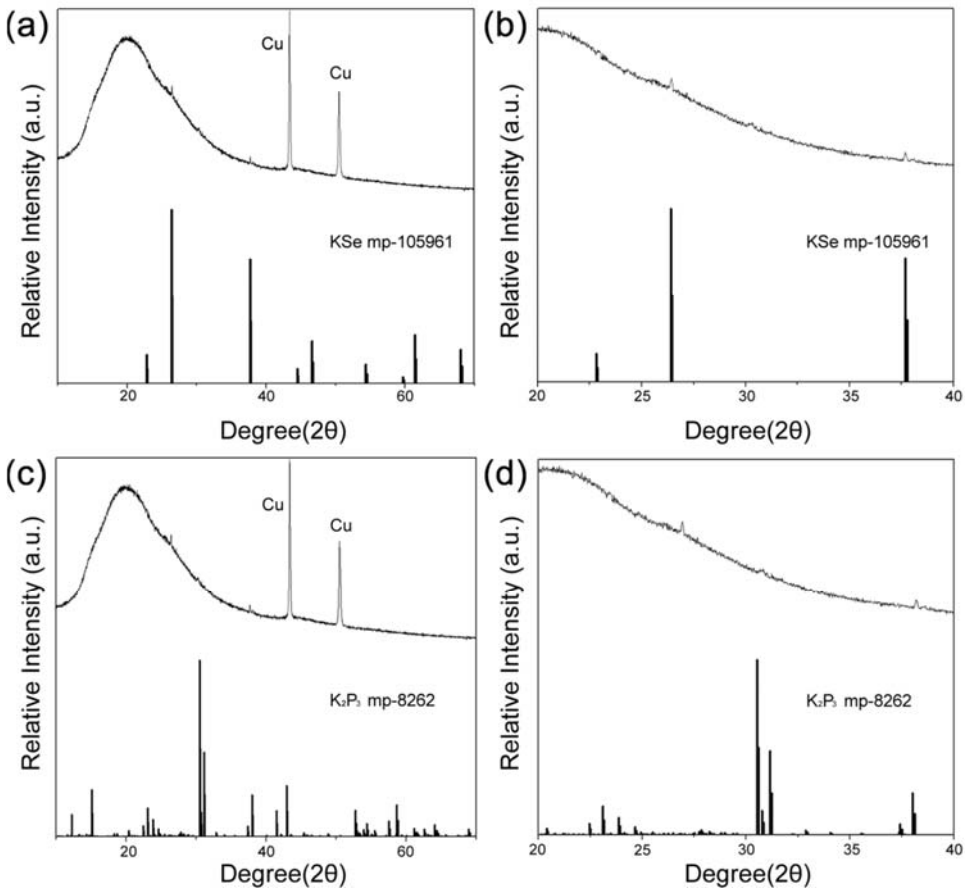

Fig. S15. XRD pattern of cycled Se-2P/C@30h electrode after it was discharged to 0.01 V: (a-b) comparison with KSe mp-105961; (c-d) comparison with K_2P_3 mp-8262.

In Fig. S15a-b, it is observed that the peaks located at 26.13º and 37.47º are corresponded to the characteristic peaks (200) and (220) of KSe (Material ID: mp-105961). Fig. S15c-d shows that the peak at 30.71º is corresponded to the characteristic peak (222) of K_2P_3 (Material ID: mp-8262). These KSe and K_2P_3 phase can be found on the Material Project, which could be searched on the science website [8].

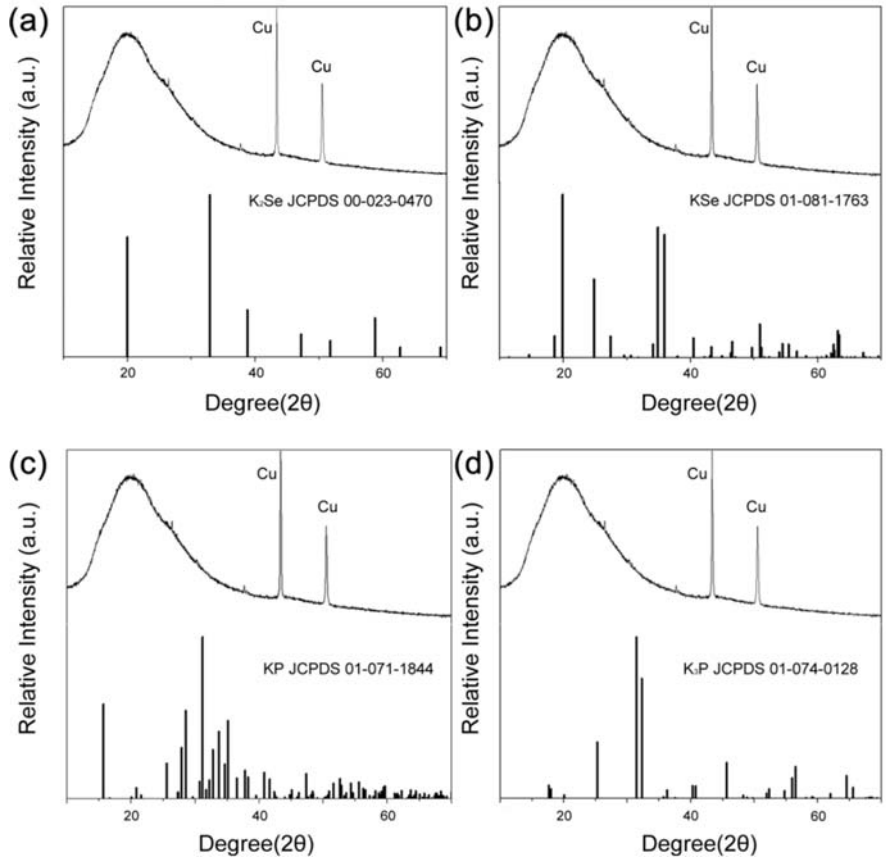

Fig. S16. XRD pattern of cycled Se-2P/C@30h electrode after it was discharged to 0.01 V: (a) comparison with K_2Se (JCPDS 00-023-0470); (b) comparison with KSe (JCPDS 01-081-1763); (c) comparison with KP (JCPDS 01-071-1844); (d) comparison with K_3P (JCPDS 01-074-0128).

In Fig.S16a-b, the KSe (JCPDS: 00-023-0470), KSe (JCPDS: 01-081-1763), KP (JCPDS: 01-071-1844) and K_3P (JCPDS: 01-074-0128) do not match with the peaks existing on the Se-2P/C@30h electrode after it was discharged to 0.01 V.

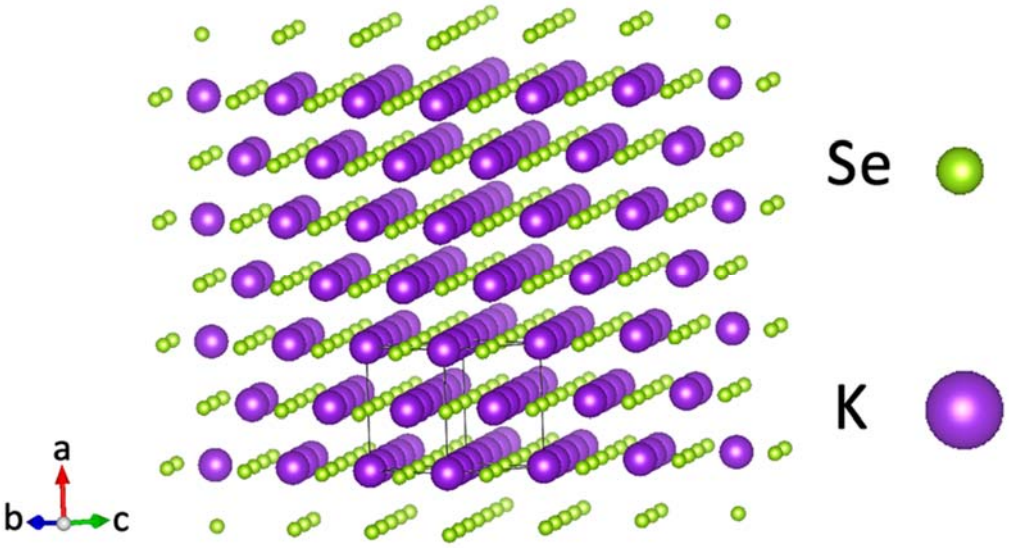

Fig. S17. A schematic of the crystal structure for KSe (Material ID: mp-1059621).

Table S5. Structural parameters and atomic position of KSe (Material ID: mp-1059621).

Atom	Site	x	y	z	Occ	B
K	4a	0.000000	0.000000	0.000000	1	1
Se	4b	0.000000	0.000000	0.500000	1	1

Space group	F m -3 m
a (Å)	6.7454
Cell Volume (Å^3)	306.922

Table S6. The calculating powder diffraction parameters of KSe (Material ID: mp-1059621).

h	k	l	d (Å)	2θ	I
1	1	1	3.894473	22.81577	16.13366
1	1	1	3.894473	22.87177	8.0312
2	0	0	3.372713	26.4047	100
2	0	0	3.372713	26.46981	49.75117
2	2	0	2.384868	37.68809	71.46987
2	2	0	2.384868	37.78282	35.54625
3	1	1	2.033822	44.51172	8.17225
3	1	1	2.033822	44.62531	4.06589
2	2	2	1.947237	46.60486	24.03528
2	2	2	1.947237	46.72442	11.95131
4	0	0	1.686356	54.35924	10.63216
4	0	0	1.686356	54.50179	5.28604
3	3	1	1.547507	59.70464	3.42111
3	3	1	1.547507	59.86398	1.70178
4	2	0	1.508323	61.42058	27.59441
4	2	0	1.508323	61.5855	13.71962
4	2	2	1.376904	68.03428	19.18602
4	2	2	1.376904	68.22169	9.54143
3	3	3	1.298158	72.79399	0.60563
5	1	1	1.298158	72.79399	1.8169
3	3	3	1.298158	72.99871	0.30146
5	1	1	1.298158	72.99871	0.90438
4	4	0	1.192434	80.47939	5.45834
4	4	0	1.192434	80.71445	2.7182
5	3	1	1.140185	84.99982	2.24812
5	3	1	1.140185	85.25438	1.12115
4	4	2	1.124238	86.49832	8.84496
6	0	0	1.124238	86.49832	2.21124
4	4	2	1.124238	86.75966	4.4099
6	0	0	1.124238	86.75966	1.10248

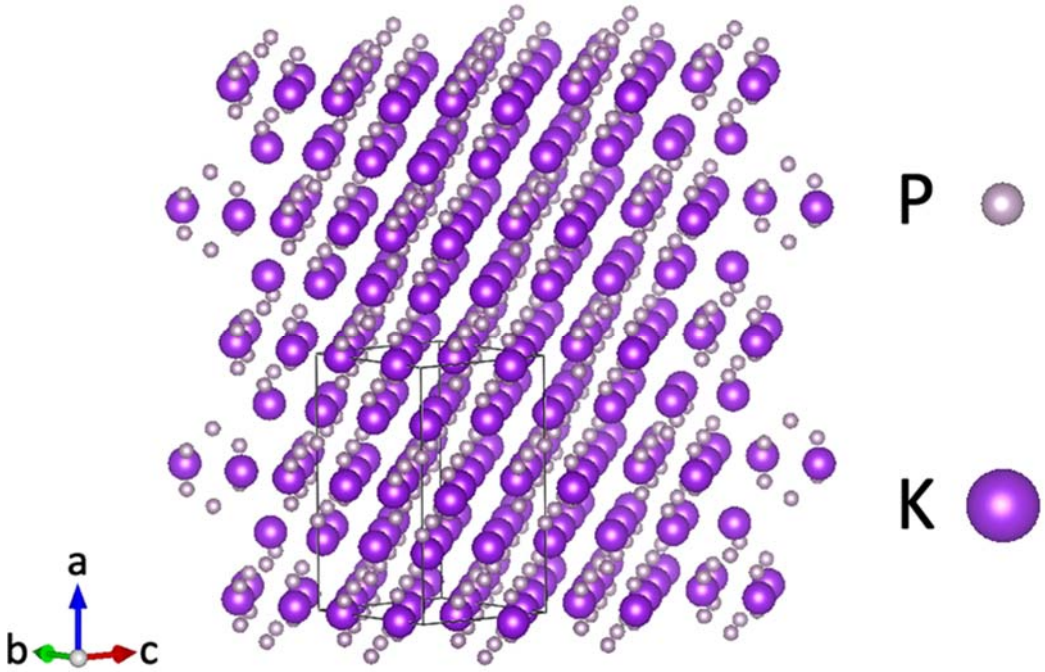

Fig. S18. A schematic of the crystal structure for K_2P_3 (Material ID: mp-8262).

Table S7. Structural parameters and atomic position of K_2P_3 (Material ID: mp-8262).

Atom	Site	x	y	z	Occ	B
K_1	8h	0.000000	0.228497	0.000000	1	1
K_2	8f	0.250000	0.250000	0.250000	1	1
P_1	16n	0.215724	0.000000	0.424809	1	1
P_2	8i	0.000000	0.000000	0.348797	1	1

Space group	F m m m
a (Å)	8.69801
b (Å)	9.45838
c (Å)	14.42978
Cell Volume ($Å^3$)	1187.1249

Table S8. The calculating powder diffraction parameters of K_2P_3 (Material ID: mp-8262).

h	k	l	d (Å)	2θ	I
0	0	2	7.214892	12.25771	12.49462
0	0	2	7.214892	12.28751	6.21728
1	1	1	5.852204	15.12701	26.51961
1	1	1	5.852204	15.16386	13.19582
0	2	0	4.729188	18.74836	1.50484
0	2	0	4.729188	18.79417	0.74923
2	0	0	4.349006	20.40412	3.31056
2	0	0	4.349006	20.45407	1.64711
0	2	2	3.955232	22.46068	6.12773
0	2	2	3.955232	22.51579	3.04859
1	1	3	3.845594	23.10974	16.09839
1	1	3	3.845594	23.16648	8.00887
2	0	2	3.724663	23.87092	9.56737
2	0	2	3.724663	23.92958	4.75887
0	0	4	3.607446	24.65855	4.1987
0	0	4	3.607446	24.71921	2.08841
2	2	0	3.201191	27.84722	2.45126
2	2	0	3.201191	27.91603	1.21938
2	2	2	2.926102	30.52599	100
2	2	2	2.926102	30.60173	49.73781
1	3	1	2.903457	30.76994	13.52069
1	3	1	2.903457	30.84631	6.72505
0	2	4	2.868233	31.15736	47.74556
0	2	4	2.868233	31.23474	23.74718
2	0	4	2.776561	32.21355	0.13014
2	0	4	2.776561	32.29369	0.06473
3	1	1	2.722249	32.87429	2.24318
3	1	1	2.722249	32.95617	1.11568
1	1	5	2.631014	34.04838	0.88958
1	1	5	2.631014	34.13337	0.44243
1	3	3	2.523417	35.54753	0.53088
1	3	3	2.523417	35.6365	0.26408
0	0	6	2.404964	37.36146	0.95886
3	1	3	2.401722	37.41377	5.80258
0	0	6	2.404964	37.4553	0.47685
3	1	3	2.401722	37.50775	2.88566
2	2	4	2.394388	37.53263	0.0982
2	2	4	2.394388	37.62694	0.04884
0	4	0	2.364594	38.02357	23.61925
0	4	0	2.364594	38.11921	11.74536
0	4	2	2.246994	40.09657	0.5772

0	4	2	2.246994	40.19786	0.28704
4	0	0	2.174503	41.49378	14.58097
4	0	0	2.174503	41.59892	7.25001
0	2	6	2.143696	42.11824	1.18499
0	2	6	2.143696	42.22512	0.58924
3	3	1	2.111163	42.79896	0.00291
3	3	1	2.111163	42.90773	0.00145
2	0	6	2.104603	42.93895	28.84446
2	0	6	2.104603	43.04812	14.3416
4	0	2	2.081997	43.42871	0.1977
2	4	0	2.077389	43.52996	1.02581
4	0	2	2.081997	43.53926	0.0983
2	4	0	2.077389	43.64079	0.51005
1	3	5	2.067747	43.74339	0.13012
1	3	5	2.067747	43.85481	0.06469
3	1	5	1.999182	45.32545	0.9121
2	4	2	1.996286	45.39486	1.9879
3	1	5	1.999182	45.44135	0.45351
2	4	2	1.996286	45.51096	0.98817
0	4	4	1.977616	45.84773	0.90393
4	2	0	1.975662	45.89567	0.07526
0	4	4	1.977616	45.96512	0.44933
4	2	0	1.975662	46.0132	0.03742
1	1	7	1.962198	46.22879	0.1863
1	1	7	1.962198	46.34727	0.09263
3	3	3	1.950735	46.51636	0.63459
3	3	3	1.950735	46.63567	0.31555
2	2	6	1.922797	47.23295	0.01681
2	2	6	1.922797	47.35432	0.00842
4	2	2	1.905512	47.68783	0.3554
4	2	2	1.905512	47.81052	0.17669
4	0	4	1.862331	48.86481	1.38008
4	0	4	1.862331	48.99092	0.68599
1	5	1	1.833483	49.68527	0.0301
1	5	1	1.833483	49.81379	0.01498
0	0	8	1.803723	50.56214	0.47756
2	4	4	1.800231	50.66714	0.20129
0	0	8	1.803723	50.69325	0.23737
2	4	4	1.800231	50.79856	0.10006
4	2	4	1.732814	52.78718	14.81521
4	2	4	1.732814	52.92495	7.36441
1	5	3	1.725438	53.03042	3.01899
1	5	3	1.725438	53.16892	1.50072
3	3	5	1.715922	53.34769	2.01568

3	3	5	1.715922	53.48715	1.00199
5	1	1	1.699004	53.92163	3.86143
5	1	1	1.699004	54.06285	1.91961
1	3	7	1.692365	54.15043	1.01087
1	3	7	1.692365	54.29234	0.50249
0	4	6	1.686112	54.36776	0.75648
0	2	8	1.685305	54.39596	7.21442
0	4	6	1.686112	54.51033	0.37605
0	2	8	1.685305	54.53862	3.58612
2	0	8	1.66611	55.07541	1.34622
2	0	8	1.66611	55.22016	0.66922
3	1	7	1.654152	55.50779	3.40175
3	1	7	1.654152	55.65387	1.69106
4	0	6	1.612944	57.05384	0.06754
5	1	3	1.611965	57.09168	0.60209
4	0	6	1.612944	57.20475	0.03357
5	1	3	1.611965	57.24271	0.29929
4	4	0	1.600596	57.53495	8.62432
4	4	0	1.600596	57.68737	4.28695
0	6	0	1.576396	58.50298	0.14056
3	5	1	1.574823	58.5671	1.22872
0	6	0	1.576396	58.65847	0.06991
2	4	6	1.572095	58.67866	17.94993
2	2	8	1.57144	58.70549	2.28507
3	5	1	1.574823	58.72279	0.61076
2	4	6	1.572095	58.83471	8.92255
2	2	8	1.57144	58.86163	1.13592
4	4	2	1.562605	59.07019	0.0489
4	4	2	1.562605	59.22749	0.02431
1	5	5	1.556553	59.32277	0.7982
1	1	9	1.555283	59.37607	0.71448
1	5	5	1.556553	59.48088	0.39676
1	1	9	1.555283	59.53435	0.35517
0	6	2	1.540064	60.02271	0.52824
0	6	2	1.540064	60.18308	0.26259
4	2	6	1.526597	60.60748	0.08671
4	2	6	1.526597	60.76974	0.0431
5	3	1	1.514715	61.13353	4.51392
5	3	1	1.514715	61.29751	2.24391
3	5	3	1.504762	61.58172	2.33625
3	5	3	1.504762	61.74717	1.16135
3	3	7	1.482674	62.60173	4.06867
2	6	0	1.48204	62.63153	0.05469
3	3	7	1.482674	62.77055	2.02264

2	6	0	1.48204	62.80045	0.02719
5	1	5	1.471719	63.12108	1.10734
5	1	5	1.471719	63.29163	0.5505
4	4	4	1.463051	63.53857	0.71351
4	4	4	1.463051	63.71051	0.35465
5	3	3	1.452066	64.07622	0.02187
2	6	2	1.451728	64.09288	6.70473
6	0	0	1.449669	64.19483	0.02769
5	3	3	1.452066	64.24998	0.01088
2	6	2	1.451728	64.26669	3.33306
6	0	0	1.449669	64.36899	0.01377
0	6	4	1.4445	64.45217	3.34236
0	0	10	1.442978	64.52838	0.12725
0	6	4	1.4445	64.6272	1.66158
0	0	10	1.442978	64.70367	0.06326
0	4	8	1.434116	64.97597	0.24073
0	4	8	1.434116	65.15278	0.11966
6	0	2	1.421263	65.63709	0.85635
6	0	2	1.421263	65.81616	0.42571
1	3	9	1.410222	66.21664	0.05851
1	3	9	1.410222	66.39771	0.0291
3	5	5	1.388784	67.37395	0.00785
4	0	8	1.388281	67.40166	0.65188
3	1	9	1.387882	67.42362	0.03447
6	2	0	1.386012	67.52678	0.0565
3	5	5	1.388784	67.55905	0.00391
4	0	8	1.388281	67.58685	0.32409
3	1	9	1.387882	67.60889	0.01714
6	2	0	1.386012	67.71241	0.0281
0	2	10	1.380162	67.85182	0.19586
0	2	10	1.380162	68.03859	0.09739
1	5	7	1.376206	68.07352	0.0306
1	5	7	1.376206	68.26108	0.01521
2	6	4	1.370861	68.37555	0.01172
2	0	10	1.36956	68.44952	0.46127
2	6	4	1.370861	68.56417	0.00583
2	0	10	1.36956	68.6384	0.22933
2	4	8	1.361976	68.88413	1.01973
6	2	2	1.361124	68.93332	4.03615
2	4	8	1.361976	69.07456	0.50709
6	2	2	1.361124	69.12393	2.00687
5	3	5	1.347036	69.75805	0.22232
6	0	4	1.345122	69.87176	0.07888
5	3	5	1.347036	69.95161	0.11057

6	0	4	1.345122	70.06574	0.03922
4	4	6	1.33247	70.63359	0.13449
4	2	8	1.332071	70.65789	4.06888
1	7	1	1.329503	70.81485	1.50735
4	4	6	1.33247	70.83033	0.06688
4	2	8	1.332071	70.85472	2.02339
1	7	1	1.329503	71.01225	0.74961
0	6	6	1.318411	71.50166	0.09178
5	1	7	1.316527	71.61975	0.35648
2	2	10	1.315507	71.68384	4.4287
0	6	6	1.318411	71.70158	0.04565
5	1	7	1.316527	71.82011	0.1773
2	2	10	1.315507	71.88443	2.20253
6	2	4	1.293805	73.07846	0.11765
6	2	4	1.293805	73.28425	0.05852
1	7	3	1.286535	73.55905	0.00405
1	1	11	1.285101	73.65464	0.0812
1	7	3	1.286535	73.76665	0.00202
1	1	11	1.285101	73.86261	0.04039
3	3	9	1.281865	73.87145	0.04799
3	3	9	1.281865	74.08023	0.02387
4	6	0	1.2763	74.24754	0.01326
5	5	1	1.275465	74.30435	0.65572
4	6	0	1.2763	74.45775	0.00661
5	5	1	1.275465	74.51479	0.32625
2	6	6	1.261708	75.25402	0.0934
2	6	6	1.261708	75.46811	0.04651
4	6	2	1.256787	75.60032	0.21347
3	5	7	1.256157	75.64493	0.59654
4	6	2	1.256787	75.81575	0.10621
3	5	7	1.256157	75.86053	0.29684
6	0	6	1.241554	76.69496	2.18506
6	0	6	1.241554	76.91468	1.08728
5	5	3	1.23738	77.00109	0.63111
6	4	0	1.235896	77.11061	0.01168
5	5	3	1.23738	77.22202	0.31406
6	4	0	1.235896	77.33197	0.00581
0	4	10	1.231742	77.4189	0.19526
0	4	10	1.231742	77.64149	0.09717
7	1	1	1.227521	77.73504	0.5426
5	3	7	1.22501	77.92449	0.03175
7	1	1	1.227521	77.9589	0.27005
5	3	7	1.22501	78.1491	0.01581
3	7	1	1.22034	78.27961	0.06888

6	4	2	1.218153	78.44712	0.72851
3	7	1	1.22034	78.50565	0.03428
6	4	2	1.218153	78.67384	0.36257
1	7	5	1.211779	78.93998	0.14214
1	5	9	1.21118	78.98669	0.70357
1	7	5	1.211779	79.16869	0.07075
1	5	9	1.21118	79.2156	0.35021
4	6	4	1.203215	79.61323	2.85973
0	0	12	1.202482	79.67147	1.34344
4	0	10	1.202335	79.68315	0.13163
6	2	6	1.200861	79.80059	0.27714
4	6	4	1.203215	79.8447	1.42359
0	0	12	1.202482	79.90319	0.66879
1	3	11	1.199572	79.90358	0.00665
4	0	10	1.202335	79.91491	0.06553
6	2	6	1.200861	80.03283	0.13795
4	4	8	1.197194	80.09436	0.55874
1	3	11	1.199572	80.13626	0.00331
4	4	8	1.197194	80.32782	0.27815
7	1	3	1.193461	80.39598	0.54037
7	1	3	1.193461	80.6307	0.26905
0	6	8	1.186966	80.92686	1.49527
3	7	3	1.186857	80.93581	0.00838
3	1	11	1.185731	81.02867	0.4008
2	4	10	1.185126	81.07866	0.38396
0	6	8	1.186966	81.1638	0.74452
3	7	3	1.186857	81.17278	0.00418
3	1	11	1.185731	81.26603	0.19958
0	8	0	1.182297	81.3134	1.46204
2	4	10	1.185126	81.31623	0.19117
0	8	0	1.182297	81.55196	0.72804
5	5	5	1.170441	82.31408	0.96019
5	1	9	1.1699	82.36035	0.62448
6	4	4	1.169184	82.42176	0.15442
5	5	5	1.170441	82.55689	0.47822
5	1	9	1.1699	82.60336	0.31103
0	8	2	1.166736	82.63255	0.00586
6	4	4	1.169184	82.66503	0.07691
0	2	12	1.165399	82.74813	0.01516
4	2	10	1.165265	82.7597	0.21578
0	8	2	1.166736	82.87673	0.00292
0	2	12	1.165399	82.9928	0.00756
4	2	10	1.165265	83.00443	0.10748
2	0	12	1.158995	83.30702	0.14344

2	0	12	1.158995	83.55412	0.07146
7	3	1	1.152338	83.89727	0.12412
7	3	1	1.152338	84.14695	0.06184
2	6	8	1.145083	84.55144	1.00308
2	6	8	1.145083	84.80401	0.49981
2	8	0	1.14089	84.93496	0.24028
2	8	0	1.14089	85.18923	0.11973
7	1	5	1.133063	85.66154	0.37586
7	1	5	1.133063	85.91908	0.18733
6	0	8	1.129954	85.95424	0.05316
3	7	5	1.127408	86.19557	0.76317
4	6	6	1.12738	86.19822	0.0004
6	0	8	1.129954	86.2131	0.0265
3	5	9	1.126925	86.24152	0.16005
2	8	2	1.126888	86.24506	0.03211
2	2	12	1.125683	86.35994	0.24049
3	7	5	1.127408	86.45553	0.38039
4	6	6	1.12738	86.45819	0.0002
3	5	9	1.126925	86.50169	0.07977
2	8	2	1.126888	86.50525	0.016
7	3	3	1.124021	86.51906	0.13702
0	8	4	1.123497	86.56938	0.01358
2	2	12	1.125683	86.62065	0.11988
7	3	3	1.124021	86.78049	0.06831
0	8	4	1.123497	86.83105	0.00677
1	7	7	1.120648	86.84412	0.47271
1	7	7	1.120648	87.10705	0.23565
3	3	11	1.117557	87.1444	0.07956
3	3	11	1.117557	87.40872	0.03967
5	3	9	1.104273	88.46308	0.1878
5	3	9	1.104273	88.73357	0.09367
6	4	6	1.099242	88.97477	2.5982
6	2	8	1.099018	88.9977	0.11008
6	4	6	1.099242	89.24769	1.29585
6	2	8	1.099018	89.27073	0.05491
1	1	13	1.093669	89.54982	0.3077
1	1	13	1.093669	89.8255	0.1535

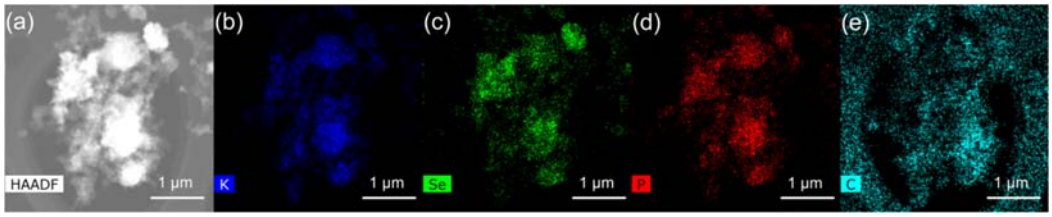

Fig. S19. EDS maps of the cycled Se-2P/C@30h electrode after it was discharged to 0.01 V.

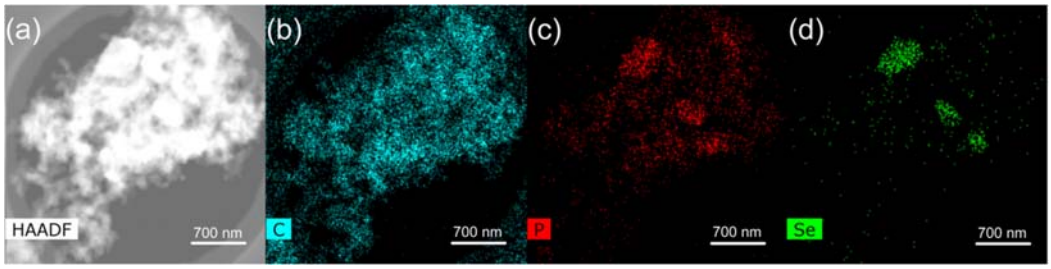

Fig. S20. EDS maps of the cycled Se-2P/C@30h electrode after it was charged to 3 V.

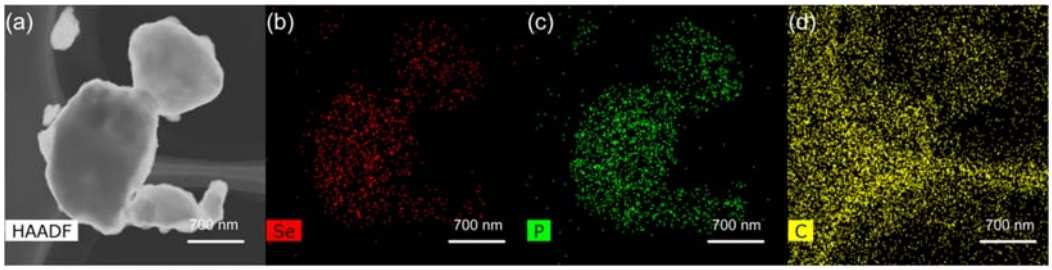

Fig. S21. EDS maps of the Se-2P/C@30h electrode in the depotassiation state after 150 cycles.

References

[1] W. Zhang, Z. Wu, J. Zhang, G. Liu, N. Yang, R. Liu, R. Liu, W. Pang, W. Li, Z. Guo, Unraveling the effect of salt chemistry on long-durability high-phosphorus-concentration anode for potassium ion batteries, Nano Energy 53(2018) 967-974.

[2] W. Zhang, W. Pang, V. Sencadas, Z. Guo, Understanding high-energy-density Sn_4P_3 anodes for potassium-ion batteries, Joule 2.8 (2018): 1534-1547.

[3] W. Zhang, J. Mao, S. Li, Z. Chen, Z. Guo, Phosphorus-based alloy materials for advanced potassium-ion battery anode, J. Am. Chem. Soc. 139.9(2017) 3316-3319.

[4] I. Sultana, T. Ramireddy, M. M. Rahman, Y. Chen, A. M. Glushenkov, Tin-based composite anodes for potassium-ion batteries, Chem. Commun. 52.59(2016) 9279-9282.

[5] K. Huang, Z. Xing, L. Wang, X. Wu, W. Zhao, X. Qi, H. Wang, Z. Ju, Direct synthesis of 3D hierarchically porous carbon/Sn composites via in situ generated NaCl crystals as templates for potassium-ion batteries anode, J. Mater. Chem. A 6(2018) 434-442.

[6] Q. Zhang, J. Mao, W. Pang, T. Zheng, V. Secadas, Y. Chen, Y. Liu, Z. Guo, Boosting the Potassium Storage Performance of Alloy‐Based Anode Materials via Electrolyte Salt Chemistry, Adv. Energy Mater. 8(2018) 1703288.

[7] X. Ren, Q. Zhao, D. W. McCulloch, Y. Wu, MoS_2 as a long-life host material for potassium ion intercalation, Nano Res. 10.4(2017) 1313-1321.

[8] https://materialsproject.org/#search/materials/